國立交通大學

應用化學系碩士班

碩士論文

一維奈米結構釩氧化物VO_2， V_2O_3和β-$Na_xV_2O_5$之成長及其鑑定

Growth of Characterization of Nearly-Aligned VO_2, V_2O_3 and β-$Na_xV_2O_5$ Nanowires

研究生：柯智軒

指導教授：李積琛 博士

中華民國一百年七月

一維奈米結構釩氧化物VO_2， V_2O_3和β-$Na_xV_2O_5$之成長及其鑑定

Growth of Characterization of Nearly-Aligned VO_2, V_2O_3 and β-$Na_xV_2O_5$ Nanowires

研究生:柯智軒　Student : Jhih-Syuan Ke

指導教授: 李積琛 博士　Advisor : Chih-Shen Lee

國立交通大學

應用化學系碩士班

碩士論文

A Thesis
Submitted to M. S. Program
Department of Applied Chemistry

College of Science

National Chiao Tung University

in Partial Fulfillment of the Requirements

for the Degree of Master of Science

in

Applied Chemistry

July 2011

Hsinchu, Taiwan, Republic of China

中華民國一百年七月

Contents

Growth of Characterization of Nearly-Aligned VO_2, V_2O_3 and β-$Na_xV_2O_5$ Nanowires

Student: Jhih-Syuan Ke Advisor: Dr. Chi-Shen Lee

M. S. Program, Department of Applied Chemistry

National Chiao Tung University

English Abstract

We report a deposition process to prepare nearly aligned binary and ternary vanadium oxides nanowires, including VO_2(R), VO_2(B), V_2O_3, and β-$Na_xV_2O_5$. In the first section, VO_2(R), VO_2(B), and V_2O_3 nanowires were prepared by reducing the precursor of V_2O_5 nanowires with controlled concentration of reducing gas flow and reduced period. The large portions of NWs microstructure are successfully preserved during the reduction, and are still nearly vertical-aligned on the surface. The growth directions of these reducing products were influenced by the growth direction of the original phase, V_2O_5 NWs. On the basis of the growth direction of each product, possible mechanisms of conversion during reduction reaction are proposed. In the second section, β-$Na_xV_2O_5$ nanowires were prepared via a route combined the original thermal evaporation procedure with additive pre-treatment of the surfaces of substrates. The sodium silicate, source of the sodium, was first coated on the substrates and the amount of precursor was carefully controlled on a Na^+-free substrate. The length of the β-$Na_{0.24}V_2O_5$ wires could be controlled in the range of 5-25μm by changing the reaction condition, which grew along the [100] direction.

X-ray powder diffraction (XRD) and transmission electron microscopy (TEM) were used to confirm the crystallinity of oxide nanowires. The effect of the controlled amount of deposited material and morphology were studied. A possible formation mechanism was proposed. The field emission properties of these binary and ternary vanadium oxides nanowires have been investigated. The results show that the as-prepared NWs possess excellent field emission performances with low turn-on field, large emission current density and linear Fowler-Nordheim behaviors. The studies suggest that these 1D nanomaterials could serve as promising candidates for future field emission devices.

一維奈米結構釩氧化物VO_2， V_2O_3和β-$Na_xV_2O_5$之成長及其鑑定

學生：柯智軒　　　　　　　　　　　　　　　　指導教授：李積琛 博士

國立交通大學應用化學系碩士班

Chinese Abstract

在這份研究報告當中，我們提出一套新穎的合成方法來沉積接近垂直成長之奈米線薄膜。能經由此套合成方法製備出的材料有R相之釩氧化二釩(VO_2(R))、B相之二氧化釩(VO_2(B))、三氧化二釩(V_2O_3))以及β相的鈉釩氧化物(β-$Na_xV_2O_5$)奈米線，這套合成方法能細分成兩個部分。在第一部分當中，V_2O_5奈米線是作為一前驅產物，先一步的由熱蒸鍍合成法製備而得。接著再進一步的將V_2O_5奈米線在還原氣體的氛圍下加熱，進行還原反應。在此還原反應中，有影響的可變參數為還原溫度、還原反應時間以及還原氣體的組成。經由準確的調控反應參數能夠成功的製備出三個具有不同結晶性釩氧化物的奈米線，其中包括VO_2(R)，VO_2(B)和 V_2O_3。在還原反應之後，獲得的釩氧化物能夠順利得保有原先的奈米線構型，且奈米線也仍然是近乎垂直的排列在基板上。在研究奈米線的結晶性的過程當中，我們發現被還原的釩氧化物其奈米線的成長方向會受到最原始的V_2O_5奈米線的成長方向所影響。因此，在此論點的基礎下，我們考慮各個奈米線的成長方向，成功的建構出在還原反應裡可能進行的轉變機制。

再另一個部分中，在原有的熱蒸鍍合成法中加入「基板前處理」後，β-$Na_xV_2O_5$奈米線就能成功的被製備獲得。在此系統中，矽酸鈉鹽是作為提供鈉離子來源的反應前驅物，因此我們在不含鈉的基板上先一步的沉積一層矽酸鈉鹽薄膜並精準的控制其鈉的含量。接著在熱蒸鍍合成法中，釩氧錯合物會被蒸氣攜帶至基板上再與基板上的鈉離子反應，進一步的生成出β-$Na_xV_2O_5$奈米線。經由X光粉末繞射與穿透式電子顯微鏡的量測之後，能夠推測出β-$Na_xV_2O_5$奈米線是沿著[100]的方向成長。在實驗的過程當中，我們發現到會影響此反應的可變實驗參數有反應溫度，熱蒸鍍時所使用的釩氧離子溶液的濃

度以及所使用的矽酸鈉鹽溶液的濃度。經由調控這些參數，能夠控制成長在基板上的奈米線長度。最後在研究報告當中，我們將提出其可能的成長機制。

經由探討各個奈米線材的電子場發射性質，顯示出各個材料本身的性質與其場發射特性具有相當的關連性。此報告中所製備出的奈米線皆具有低觸發電壓(turn-on field)、高最大發射電流密度(emission current density)。製備出的奈米線材中，V_2O_3奈米線是有較好的電子場發射性質，其觸發電場值為 5.2V/μm，而在電場值 8.3V/μm的作用底下所測得的最大發射電流密度為 8.3mA/cm^2。這些研究結果皆顯示出，釩氧化物奈米現在未來的場發射元件上具有相當大的發展潛力。

Acknowledgements

待在交大裡的時間算一算大概有兩千多個日子，六年的歲月真的很長，長到自己覺得很膩、了無新意、很想離開，但是一旦到了要離開的日子，卻又感到分外的不捨，會有這樣的惆悵情感應該不是我喜歡交大這所大學，而是我捨不得曾經有你們存在的交大!

在這段歲月裡要感謝的人真的很多，首先我想要感謝的是我的老闆 李積琛老師，老師在研究這條路上給予我很多的指導與幫助，而且認同我所做的實驗成果，冀望我能夠投稿國外的學術期刊，對於這份信任我真的感到相當的開心、光榮然後是感謝。接著，要感謝裘性天 老師以及孫建文 老師在百忙之中抽空來聆聽我的碩士研究成果報告，給予我很多寶貴的建議以及能夠改進的地方，讓我的碩士論文的品質能夠更加提升。

充滿笑聲的實驗室生活也是讓人難以忘懷的，感謝在這實驗室內陪我一同奮鬥的好夥伴們：實驗室的大長老—擁有處女座細膩、認真特質的呆呆，真的很感謝您！不論是實驗、論文、生活上你都給予過我很多的幫助，真的感謝，每次去台中剪頭髮都少不了你的陪伴，剪個頭髮都像是去台中出遊相當有趣，有機會再去找你玩吧！；很會照（ㄊ一ㄠˊ)顧（ㄎㄢˇ）學弟妹的阿明，欠你的十分鐘揶揄時間你到底要不要用掉呢？一直欠著很難受耶 XD，前陣子還有一起相約去游泳的時候，在走去游泳的路上的談心時間，感覺真的挺不賴的！從跟你的聊天當中我獲得很多，不僅僅是學術上、待人處事還有一些有的沒的（你懂得!)，如果我退伍後還沒閃光再一起去聯誼吧；總是充滿自信的郝哥，感謝你在實驗上給我的建議，但是或許我能力不足，總是沒辦法順利的達成你給的建議，另外也感謝你介紹我很多相當實用的東西，省去我不少爬文的時間；柔情鐵漢的小 Ju，雖然你講的話很 A，但是真的都很好笑，沒有你的 A 笑話和超強的拳機火力支援，我的碩一生活會黯淡不少；行動力超強的佳芬學姐，學姐的積極與作事的態度都讓我相當的敬佩！妳超強的外語能力也讓我讚嘆不已，妳是我學習的楷模；酷愛 MLB 的家瑜學姐，在跟妳聊到 MLB 時，妳興奮的神情讓我相當的難忘，妳大概是我認識的第一個會看 MLB 的女生吧；同學好幾年的陳拔刺，你真的很黑又很壯！強大的運動能力讓我很羨慕 XD，其實我是個內向的小朋友，剛進實驗室的時候，你的存在讓我安心不少，能夠和你一起熟悉這個陌生環境、成長茁壯到變成畢業學長姐，真的很開心也很感謝！另外，也感謝你能讓我傾吐心事，變成真正的交心朋友，不過還是建議你可以再八卦一點，這樣我說起故事來會比較賣力 XD；打桌球超帥的書維哥，你的幽默常常帶給實驗室歡笑聲，你的心思細膩常常發現到我的不開心，能跟你和拔刺當同學真的很棒！另外偷偷說，我常常把你當成我的目標，你的能力與認真的態度激勵我不少，你的存在讓我的怠惰收斂許多，真的很感謝；一點都不黑而且很可愛的王允欣，果然叫妳還是要叫全名感覺才對味呀！雖然你是個學妹，但妳是跟我們三個一起適應實驗室的好夥伴，所以在我的認知裡妳一直都是跟我同屆吧，在這邊允許妳可以叫我柯智軒 XD！妳是個貼心的好女孩，時常被妳的貼心舉動感動到，能夠變成妳的好姐妹、好哥們真的深感榮幸！祝福妳；體魄愈來愈健壯的亞軍，你一直都是個嗨咖，在碩一的時候一直是大家揶揄的對象，升上碩二之後，砲火好像少了很多！實在很可惜，沒辦法再看到你以一擋百

的氣勢 XD，雖然跟你相識只有一年，但是跟你聊天都能很盡興；漸漸顯露本性的金魚，最近常常聽到妳一針見血的尾刀真的很有趣！在重訓室見識到妳的 power，真的很不簡單，看的我相當慚愧，我真的該好好努力鍛練一下了 XD；汗操很好的浩恩，你是個很好揪的運動咖，跟你打羽球、桌球都很有意思，只可惜我的籃球很弱，沒辦法跟你打得很盡興！另外你真的很愛垂坤的零食，有需要在摳我吧，隨時幫你訂；實驗室的新成員 VG、宅維、昀聲，跟你們相處的時間不長，但是感覺你們都是很有趣的人物，似乎都很享受學長們的調侃 XD，真心希望你們會喜愛這個 CSlab，Enjoy it！；活潑可愛又很 sweet 的婉欣學妹，雖然妳常常說自己很不會安慰人，但是對我來說妳的關心就是一個很好的慰藉。我們相差兩屆，沒辦法有更多的相處時光，真的感到相當的可惜，祝福妳也能有個充實且愉快的兩年實驗室生活，Cheer up！。兩年的研究生生活因為有你們，而變的精彩許多，真的很感謝大家！希望在未來還能夠有許多相聚的機會。

大學的四年生活也是讓我很感念的，即使我們大家已經經歷了一次離別，但兩年後的今天再經歷一次，依舊相當捨不得，我的好朋友們：大軒、宏憲、冠達、楊立誠、小明、百傑、阿伯、舜舜、拔刺、金毛、俊哥、李宥宗、小白、孔哥、大衛、stella、龔晏瑩、琬妤、童思頻。我們之間的友情，或許已經無法用言語表達了，除了感恩、感謝也想對你們說聲珍重再見。死黨級的高中朋友：小 a、小白沛昇、王蛋、阿鳥、月餅、黑人邵、阿甘學妹、月餅妹，你們是我一輩子的朋友，每當我遇到挫折時的一個念頭就是想要逃到你們身邊，你們的存在對我很重要，沒有你們就沒有現在的我，感謝；李大頭、張阿嘎、賴冬瓜，雖然常常被妳們凹，但是我也樂在其中，你們都是好女孩，衷心希望你們能夠順利找到自己的伴侶，如果不行，就等我開養老院養妳們好了 XD，另外我想說的是，你們是我的好哥們！而不是好姐妹 XD。摯愛的高中老師，小橘老媽佩芳、帶領我們的財哥、帥氣的堂智老師，高中這段日子對我的人生影響最大！主要的原因也是有您們，財哥的領導風格我至今都很難忘懷，您的諄諄教誨讓我受益良多，我的個性有一半都是你培養出來的，真的感謝；小橘老媽，能夠有個老師當我的乾媽真的是受寵若驚，還記得畢業的時候在妳面前哭得半死不活的，那時的心情我真的難以忘記，每次妳握著我的手跟我講道理，我真的感受到許多的溫暖。妳生了一個小女娃，變成了我的小乾妹了，過去很忙還來不及去看我的小乾妹，一定是個可愛的圓臉女孩；堂智老師，你當初帶領我們這隊去參加比賽，你的領導風格也是讓我很難忘記的 XD，每次回學校都要跟你聊一下，跟老師的相處很像朋友，這感覺很棒。雖然已經跟你們大家分開很久了，但你們依舊活在我的心中，與你們的回憶一直都是我的精神食糧，支持我、陪伴我走了相當長遠的路，真的很感謝。

最後我要感謝我的家人；首先要感謝爸爸、媽媽，您們提供我很好的成長環境，讓我可以依照自己的意願交朋友、學習、成長，最後來到新竹完成學業，你們的支持與鼓勵，真的很感謝，雖然我時常抱怨您們太囉嗦，但事實上只是我嘴巴硬，我心裡是明白你們的苦心與關心的，請原諒我這個笨兒子不太懂得表達自己的心情。溫柔的姐姐懿芯，這樣的字詞出現在妳身上，是不是很訝異呢 XD，但是這卻是我的真實感受，妳的關心都來的很及時，讓我常常心想，有個姐姐真的很好！，愛耍帥的弟弟喬譯，你酷酷的屌樣真的很妙，我覺得我是個不太會照顧人的哥哥，真的是委屈你了 XD，現在我們同時

在家睡覺的時間變少了，真的很懷念過去，睡前關燈的聊天時光，聊聊今天又作了哪些事阿、哪個學妹真的很可愛阿，你想追哪個女生阿之類的事情，但是現在不要跟我聊你女朋友，太閃了，我可受不了！

我今年24歲，在交大完成了碩士學位，回想過去，一路上跌跌撞撞，但因為有大家的支持與陪伴，這條路我走得很開心，真的很感謝大家。關於你們的一切都會牢記在我的心中，成為我向未來邁進的原動力。

List of Tables

List of Figures

Chapter 1.

Introduction

1.1 Brief review of 1D Nanomaterials

In the past decades, the word "nanotechnology" has been widely mentioned, which means any technology based on nano-scaled materials for any application in the real world. Nanotechnology includes the production and application of physical, chemical, electronic, and biological systems at scales ranging from 1 to 100 nanometers, and the length of 1 nm equals a row of 10 hydrogen atoms. When scale size of material was shrunk to nano-level, the properties of materials behave differently compared to previously bulk ones. For example, gold shows the various color (orange, red, purple, blue) when particle size was changed from 1 to 500 nm.[1] The energy band gap of Si rose from 1.12 eV to 2.60 eV when the size scale of Si was lowered down to $3nm^3$.[2]

Investigation of one-dimension (1D) nanomaterials was one portion of nanoscale materials. It is generally accepted that 1D nanostructures are more prone to charge transport than the bulk crystalline structures. In addition, 1D nanomaterials can demonstrate the characteristics of field emission owing to quantum tunneling effect.[3-4] They are also expected to as potential candidates for both interconnect[5] and functional units in fabricating sensor,[6] electronic, optoelectronic[7], thermoelectric[8-9] and electrochemical[10-12] devices with nanoscale dimension. A wide range of metal oxide with 1D nanostructure in belt, rod, wire and nanotube[10, 13-15] forms were developed in recent years, which have raised much attention for their peculiar physical properties and their potential applications.[7, 16-19] Among these metal oxide materials, 1D nanostructure for vanadium family oxides, including binary and ternary vanadium oxide, shows diverse physical and chemical properties in electronic, thermochromic, magnetic, and optoelectronic properties for their variable oxidation states, which have been widely applied on chemical sensors[20-23], ultrafast optical switchers, electrochromic[24], thermochromic[25] devices. Furthermore, the unique structural features also allow the application on rechargeable lithium battery for serving as electrodes.[11]

In this thesis, we are going to reveal the growth of kinds of vanadium family oxides with nanowires morphology, including V_2O_5, VO_2(R), VO_2(B), V_2O_3, and a ternary phase β-NaxV_2O_5, via a series of procedure containing thermal evaporation, pre-treatment of substrate, and post- reduction treatment. Crystalline, morphology, growth mechanism, and field emission properties of these nanowires and thin-film are deliberated in detail.

1.2 Family of Vanadium Oxide

Within the family of metal oxide, researches of vanadium oxides have been particularly focused in recent years for their diverse electronic, electrochromic, thermochromic, magnetic, and optoelectronic properties. Vanadium adopts different valence states, which can afford several oxidized structures. Besides, single-valence compounds such as VO, V_2O_3, VO_2 and V_2O_5, a number of mixed-valence oxides, e.g., V_6O_{13} or $V_{10}O_{24}$, have been reported.[26-27] Specifically, in this manuscript, we are interested in V_2O_5, VO_2 and V_2O_3, each of which has raised more attraction owing to their natural properties. The brief reviews of these vanadium oxides will be introduced clearly in the following section.

1.2.1 Structure, Properties and Application

1.2.1.1 V_2O_5

The structure of V_2O_5 crystallizes in orthorhombic unit cell with lattice parameter of a = 11.51 Å, b = 4.36 Å, c =3.56 Å; and the space group is $Pmn2_1$. V_2O_5 adopts a layer framework with large V–O separation along the crystallographic *b* direction. (see Figure 1.1a) In V_2O_5, V atom is coordinated with five oxygen atoms and forms a VO_5 square pyramid. Along c-axis, VO_5 square pyramids are linked by sharing edge and results in a zigzag chain structure. Two adjacent chains further share their corner oxygen atoms to form the final 2D network. (see Figure 1.1b) The fivefold coordination of vanadium with oxygen is shown in

Figure 1.2. The vanadium atom has coordinated with five oxygen atoms (V–O bond lengths vary from 1.585 Å to 2.021 Å): one with O_1 atoms, one with O_2 atoms and three with O_3 atoms. The distance between V atom and O_1* atom located at neighboring layer are too far away, leading to weak V-O_1* bond and the layer structure.[28] In the family of vanadium compound, V_2O_5 is the most stable one with the highest oxidation state and exhibits peculate layer structure, which are expected to be potential material for applications in chemical sensor, catalyst, electrochemical cell, and photoelectric devices. For example, Zarbin and co-workers fabricate V_2O_5 nanoparticles to be a cathodic material for Li^+-based batteries.[29] The study showed that the two-dimensional layer structure of V_2O_5, which favors intercalation of guest species, with high charge density and electrochemical stability makes this compound an attractive cathodic material for lithium rechargeable cells. Liu et al. had prepared the single crystal V_2O_5 nanofibers to be an ethanol sensor material.[21] The V_2O_5 nanobelts are n-type semiconductor and the charge transport proceeds via electron hoping between V^{4+}(impurity) and V^{5+} centers. When the reducing gases like ethanol are attached to the oxygen adsorbates (O^- or O_2^-) covering on the surface of V_2O_5 nanobelts by hydrogen bond, the charge carriers (V^{4+}) will increase owing to charge transfer from oxygen adsorbates to belts. The study showed that V_2O_5 have excellent potential for sensor application.

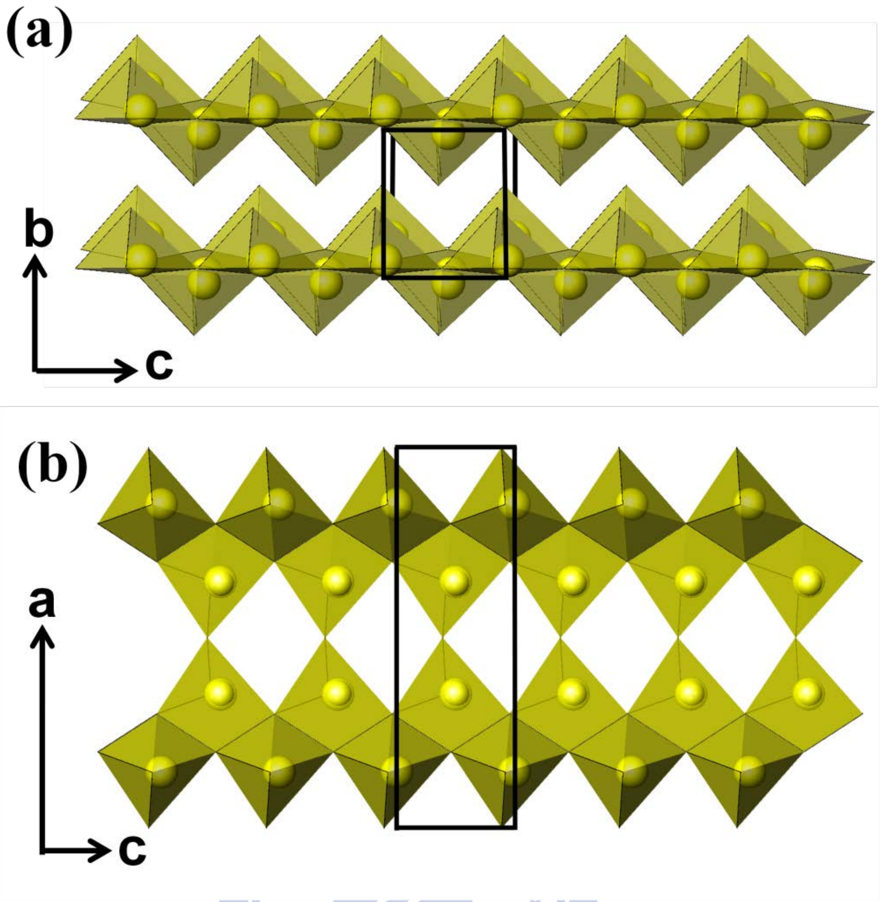

Figure 1.1 Projection of the V_2O_5 crystal structure along (a) [100] and (b) [010] axis.

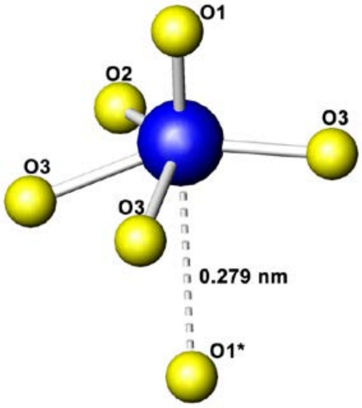

Figure 1.2 Coordination of vanadium with oxygen in vanadium pentoxide.

1.2.1.2 VO_2(R)

Vanadium dioxide (VO_2) is a traditional binary compounds with several allotropic phase, including VO_2(R), VO_2(B), VO_2(A).[30] The VO_2(R) with rutile monoclinic structure (space group : $P2_1/c$ (14)) is the most stable phase in thermodynamic concern. The projection of the VO_2(R) structure along [1 0 0] has been shown in Figure 1.3a, which gives a distorted rutile structure. In VO_2(R), vanadium atoms are coordinated with five oxygen atoms and form an octahedral geometry, with their axial axes aligned alternatively along [0 1 1] and [0 -1 1]. The octahedron is not regular which contains one shorter V-O bond length of 1.7 Å and leads to distorted rutile structure with lower symmetry. The adjacent octahedra share edges along the a-axis to form chain structure. (see Figure 1.3b) The 2_1 symmetry can be found on bc-plane and the chain structures are connected by sharing their corners to build a 3D network.

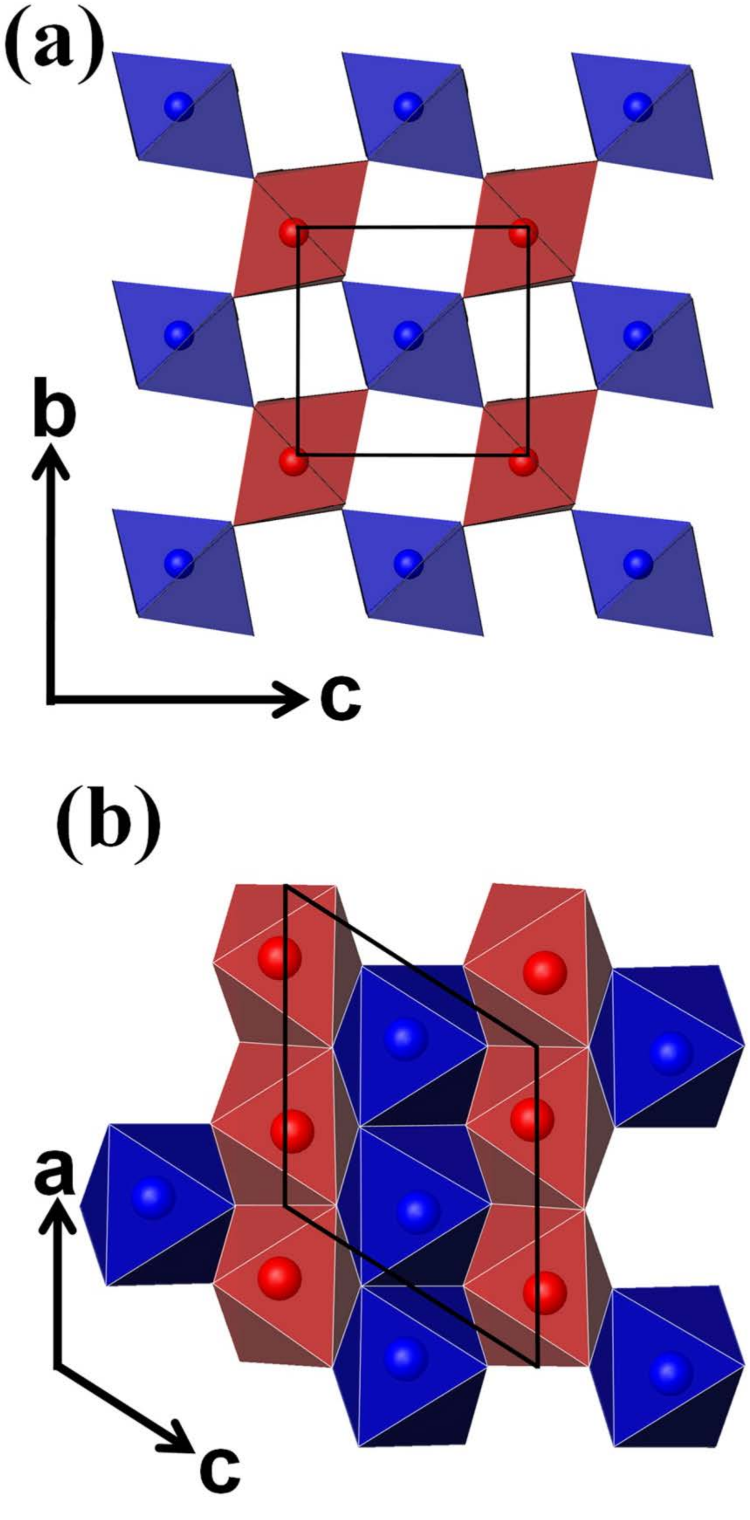

Figure 1.3 Projection of the VO_2(R) structure along (a) [100] and (b) [010] axis.

VO_2(R) possesses unique semiconductor-to-metal phase transition (SMT) at around 340K. Below the phase transition temperature, VO_2(R) shows semiconductor behavior with a monoclinic crystal (distorted rutile structure), and exhibits the optical property with IR transparent. Above the transition temperature, VO_2(R) converts to tetragonal crystal (regular rutile structure) and shows an abrupt improvement in resistivity beyond (see Figure 1.4).[31] It becomes a metal-like material, and the optical property changes to IR reflection. Accompanied with the phase transition, VO_2(R) shows not only a reversible abrupt change of electric and magnetic properties but a peculiar change of optical transmittance/reflectance in IR area, which are excellent potential for application in "smart windows".[32]

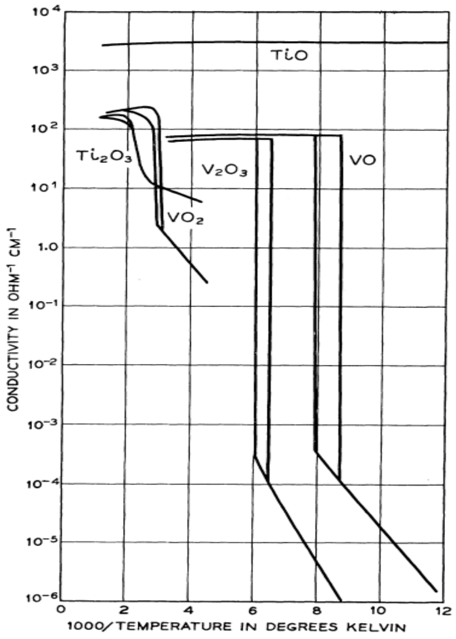

Figure 1.4 Conductivity as a function of reciprocal temperature for the lower oxides of titanium and vanadium. Measurements were made along the [100] direction in VO, and along the c axis in V_2O_3 and VO_2(R).[31]

1.2.1.3 VO_2(B)

The other phase of VO_2, VO_2(B) have a little in common with the rutile phase. VO_2(B) possesses larger monoclinic unit cell than that of VO_2(R) with lattice parameter of a = 12.03 Å, b = 3.69 Å, c = 6.42 Å, and β = 106.6° and the space group is *C*2/m(12). The VO_2(B) structure can be considered as regular-stacked identical layers of atoms along b axes. Figure 1.5 shows the arrangement of polyhedron in the (0 1 0) plane of VO_2(B) and the second layer is shifted with respect to the first one by 1/2, 1/2, 0. In this structure, V-O also forms a six-coordinated environment with slight distortion. The fourfold axes of the octahedra are more or less aligned along a single crystallographic direction, namely, [0 1 0]. Figure 1.5b shows a single layer of (0 1 0) plane for the ideal VO_2(B) structure. The structure is based on an oxygen *hcp* array with ordered oxygen vacancies, drawn here with hollow red circle. Vanadium atoms further occupy in residual octahedral sites.[30] Along b-axis, the layer structure stacks through edge-sharing to form a 3D framework.

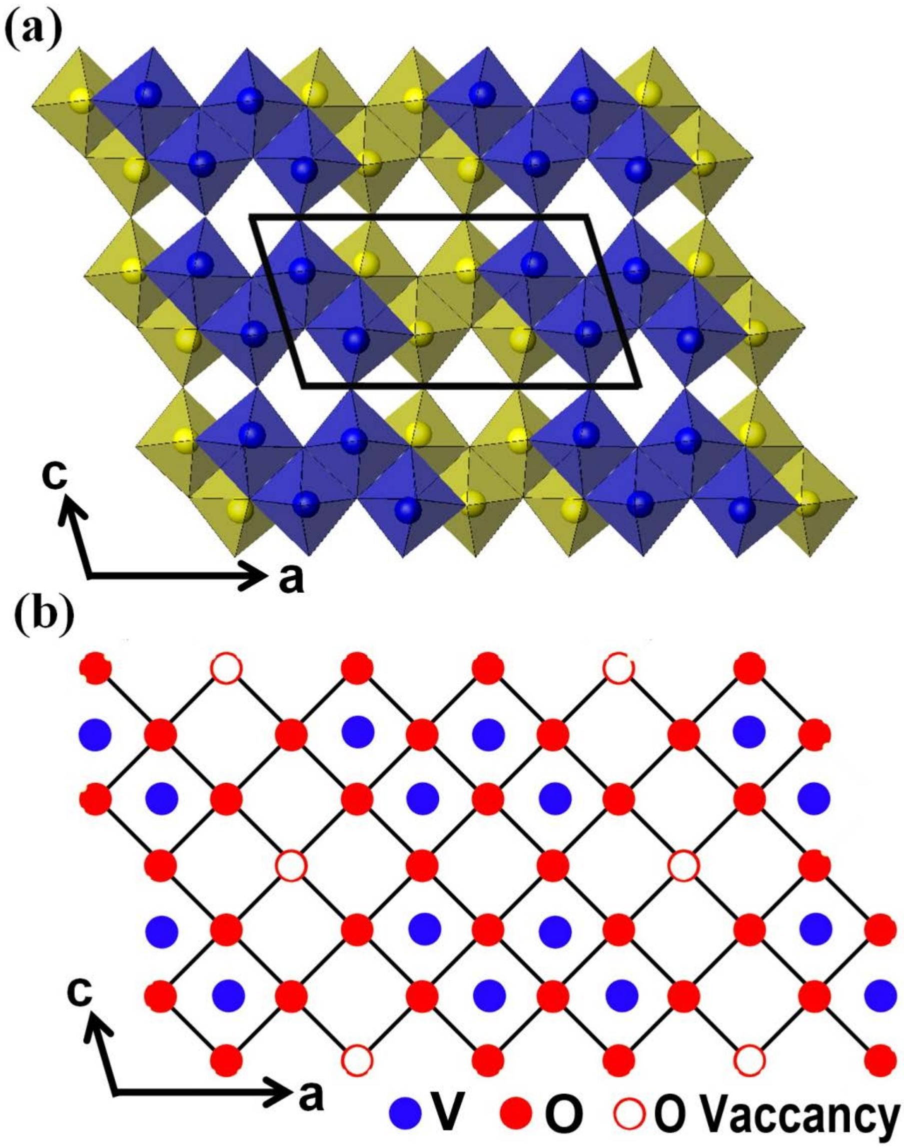

Figure 1.5 (a) Projection of the VO_2(B) structure along [010]. There are packing of edge sharing octahedra that are only linked by corners in (a,b) planes. Octahedra at y=0 and y=1/2 are, represented yellow and blue, respectively. (b) One (010) plane for the idealized VO_2(B) structure. Note that, with respect to the perfect oxygen bcc lattice, there are oxygen vacancies.

1.2.1.4 V_2O_3

V_2O_3 crystallizes in Al_2O_3 (corundum) structure with a hexagonal unit cell (space group: *R*-3c (167)) and the lattice parameters are a = 4.95 Å, b = 4.95 Å, c = 14.00 Å. Figure 1.6 shows the projection of [0 0 1] direction for the V_2O_3 structure, the structure is based on an oxygen *hcp* array with vanadium locating at 2/3 octahedral sites.

V_2O_3 also undergoes the semiconductor-to-metal phase transition (SMT) with a lower temperature (~-120°C).[31] During the phase transition process, an insulating, antiferromagnetic phase with monoclinic crystal converts to metal-like phase with corundum structure and a large change in electrical resistivity (~6 order of magnitude) is observed (see figure 1.4).

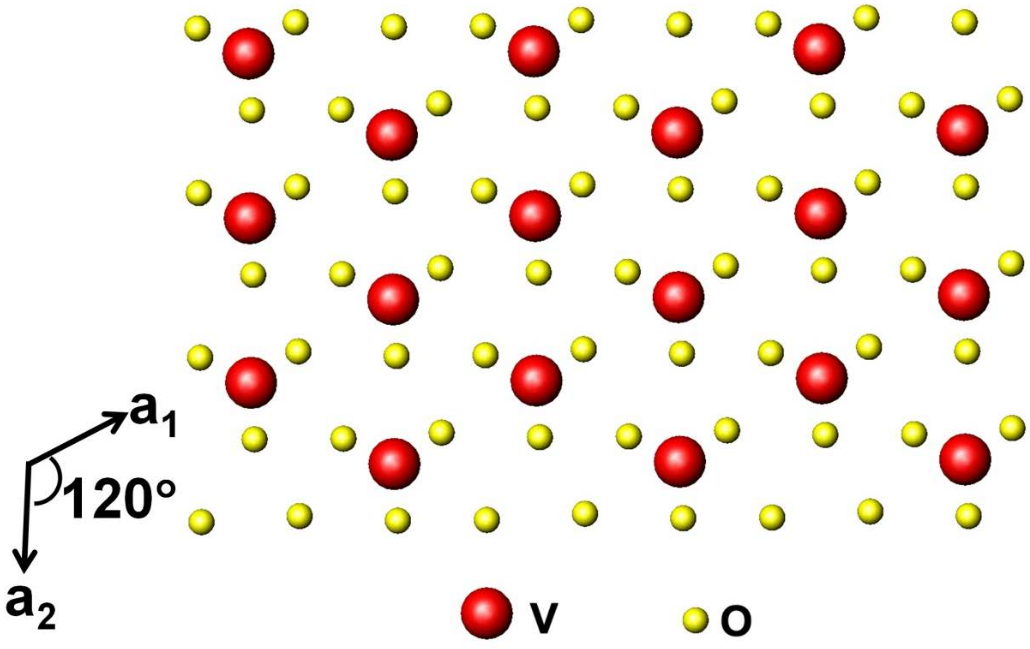

Figure 1.6 One (001) plane for the V_2O_3 structure. It shows a *hcp* arrays of O atoms (yellow) with vanadium atoms (red) occupied at 2/3 octahedral sites.

1.2.2 Literature Review of Vanadium Oxide

In the past decades, the fabrication of vanadium oxides with 1D nanostructures has been researched intensively. A variety of methods, such as CVD[33-34], hydrothermal route[23], sol-gel[20], have been developed to prepare vanadium oxides with 1D nanostructure. Table 1.1 summarizes the synthetic method for different vanadium oxides with 1D nanostructure in previous report.

In fact, V_2O_5 tends to form 1D and 2D nanomaterials owing to peculiar layer structure. Recently, lots of groups have proposed a variety of methods such as hydrothermal, sol-gel, CVD ,and electrochemical deposition to control the formation of V_2O_5 1D nanomaterials. For example, Zhou et al. grew V_2O_5 nanobelts from the reaction of ammonia metavanadate with nitric acid under thermal treatment.[35] Raible and coworkers had used sol-gel method to synthesis V_2O_5 nanofibers, whose lengths could be controlled by adjusting the reaction period.[20] Bando fabricated V_2O_5 nanowires with centimeter length via a hydrothermal reaction in an aqueous solution of V_2O_5 and H_2O_2.[36]

However, less synthetic routes are suitable to fabricate the 1D nanomaterial of reduced vanadium oxides (VO_2(R), VO_2(B), V_2O_3). A common preparative procedure for 1D nanostructure vanadium dioxides of VO_2(R) and VO_2(B) involves the hydrothermal treatment of vanadium precursor with reducing agents. For example, Sediri et al. have reported the use of aniline as both reducing agent and structural templating agent for the preparation of VO_2(B) nanoneedles from bulk V_2O_5 powder.[37] Ji and co-workers successfully fabricated single crystal VO_2(R) nanorods from the reaction of the bulk V_2O_5 powder under hydrothermal treatments in the presence of oxalic acid as reducing agent and $H_2SO_{4(aq)}$ as acidifying agent, respectively.[25] VO_2(R) with 1D nanostructures has also been synthesized via PECVD first reported by Guiton et al..[38] They had successfully deposited VO_2(R) nanowires on the Si_3N_4 substrates from VO_2(B) powder as a vanadium source under thermal evaporation (900°C-1000°C) with the assistance of the carrier gas flow of Argon gas. V_2O_3 with 1D nanostructure have only been synthesized through reduction reaction from V_2O_5 or VO_2 to V_2O_3. For example, Santulli et al. first prepared VO_2 nanorods by hydrothermal treatment, and further reduced it to V_2O_3 in the presence of reducing gas.[39] Corr and co-workers reported a systematic reduction of V_2O_5 nanoscrolls to VO_2(R) and V_2O_3 by adjusting reduction temperature and duration time.[40]

Table 1.1 Synthetic routes for different vanadium oxides with 1D nanostructure.

Material	Synthetic method
V_2O_5	Hydrothermal[23, 41], sol-gel[20], CVD[33-34], electrochemical deposition[42]
VO_2(R)	Hydrothermal[25, 43-44], CVD[38, 45], Reduction[40]
VO_2(B)	Hydrothermal[13-14, 37]
V_2O_3	Reduction[39-40]

1.3 Ternary Phase of Bronze Vanadium Oxide β-$Na_xV_2O_5$

Recently, the research in low dimensional metal oxide nanomaterial has been focused on ternary phase such as NaV_6O_{15}, Zn_2SnO_4, ZnMgO, and etc. 1D nanostructure for bronze vanadium oxides, such as β-$Na_xV_2O_5$, AgV_6O_{15}, $K_2V_8O_{21}$, CaV_6O_{16}, are well known to exhibit a wide range of practical applications.[22, 46-50] Owing to their unique structural feature combined with chemical and physical properties, they are good candidates for serving as a electrodes for rechargeable lithium battery[51], supercapacitors[52], and other else. In this study, the interesting 1D nanomaterial of β-$Na_xV_2O_5$ is the target product, and it will be introduced clearly in the following section.

1.3.1 Structure and Properties

β-$Na_xV_2O_5$ is a member of the vanadium bronzes $M_xV_2O_5$ (M=alkali, alkaline, earth and metal) family. $M_xV_2O_5$ are mixed-valence compounds, whose structure, magnetic, and electronic properties are demonstrated by the M cationic species and the concentration *x*. The β phase is located around stoichiometric concentration of $x = 0.23$-0.41. The β-$Na_xV_2O_5$ possesses a monoclinic unit cell with space group of *C*2/m, and Figure 1.7 shows the unit cell of β-$Na_{0.33}V_2O_5$ containing six NaV_6O_{15} formula unit. In the structure of β-$Na_{0.33}V_2O_5$, the V-O framework comprises of the three distinct types of double chains directed along the b axis. The V1-site has a six-coordinated octahedral geometry and forms a zigzag chain by edge-sharing. The V2 site with a similar octahedral coordination form a two-leg ladder chain of corner-sharing VO_6 octahedra, and the V3 site, having a fivefold square pyramidal coordination constructs a zigzag chain of edge-sharing VO_5 pyramids. The Na^+ ions are located in the tunnels formed by above V-O framework. In the case of concentration $x = 0.33$, the Na^+ ions occupy only one of two nearest-neighboring site A on ac plane. The electrons of the Na^+ ions are transferred into the d shells of V ions, resulting in the mixed valence states V^{4+} (d^1) and V^{5+} (d^0).[53] Precious study had demonstrated that in the high temperature, $T > 136K$, the donated electrons are situated at the V1 site, with one half of two V1 site being V^{4+}.[54] These features make β-$Na_xV_2O_5$ possesses novel physical, magnetic and superconductive properties at a critical condition.[55-57]

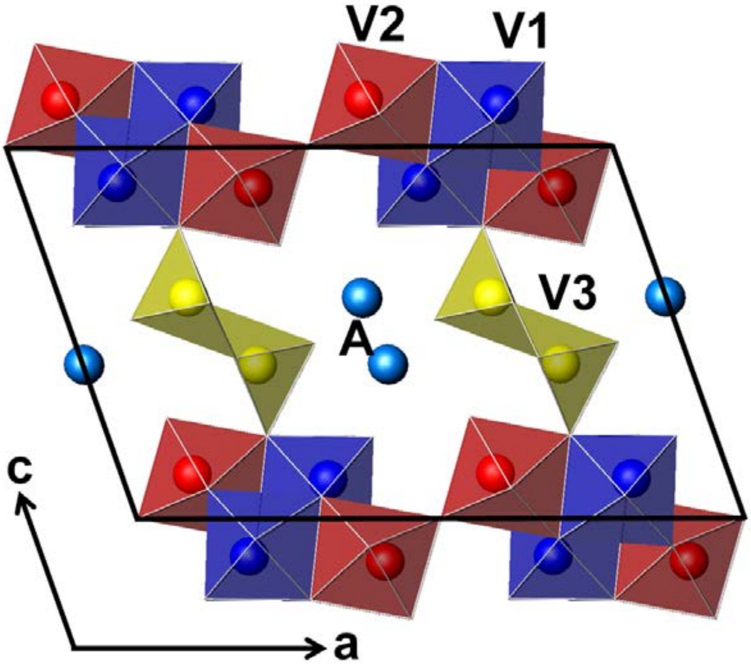

Figure 1.7 The projection of β-$Na_xV_2O_5$ crystal structure along [010].

1.3.2 Literature Review of β-$Na_xV_2O_5$

Recently, β-$Na_xV_2O_5$ has been synthesized with 1D Nanostructure through CVD and hydrothermal route. The hydrothermal method involves the reaction between V_2O_5 and sodium precursor in the presence of reducing agents. For example, Yu et al. first reported a general route for the synthesis of NaV_6O_{15} single-crystal nanowires based on hydrothermal treatment between V_2O_5 and $NaHSO_4 \cdot H_2O$.[58] They also successfully synthesized NaV_6O_{15} nanoneedles by changing the sodium precursor, $NaHSO_4 \cdot H_2O_{(aq)}$ to PSMA-$Na_{(aq)}$.[59] Zhou and co-workers successfully fabricated single crystal NaV_6O_{15} nanorods from the reaction of bulk V_2O_5 powder under hydrothermal treatment in the presence of NaCl as sodium precursor and H_2O_2 *(aq)* as reducing agent, respectively.[51]

Another preparative method based on CVD was proposed by Shivashankar[60], and the installment is shown in Figure 1.8. They successfully deposited single crystal $Na_xV_2O_5$ NWs on the surface of sodium silicate glass with the assistance of Ar/O_2 flow as carrier gas. In this study, the source of Na^+ ions were from the glass substrate that diffused into the vanadium oxide precursor and further reacted to form β-$Na_xV_2O_5$ nanowires.

1.3.3 Application

β-$Na_xV_2O_5$ possesses a more rigid 3D network that is different from the V_2O_5 with layer-type structure. The Na^+ ions are located inside the tunnels of V-O framework, resulting in the mixed-valence states $V^{5+}(d^0)$ and $V^{4+}(d^1)$. Recently, this particular feature is expected to improve the property of ions transport, charge storage and electronic transport for applications like supercapacitors and cathode material in lithium battery. For example, Zhou and co-workers used single crystalline NaV_6O_{15} nanorods to serve as a cathode material for rechargeable lithium battery and obtained a high electrochemical performance upon lithium insertion and extraction.[51] Lee et al. had successfully fabricated β-$Na_{0.33}V_2O_5$ nanobelts via hydrothermal route and used that as an electrode for supercapacitor.[52] The three dimensional framework crystal structure of the β-$Na_{0.33}V_2O_5$ nanobelts network electrode shows a high specific capacitance of 320 $F{\cdot}g^{-1}$ and only 34% degradation in specific capacitance being observed in galvanostatic cycling testing after 4000 cycles. These results suggested that the β-$Na_{0.33}V_2O_5$ nanobelt network structure is a potential energy storage material.

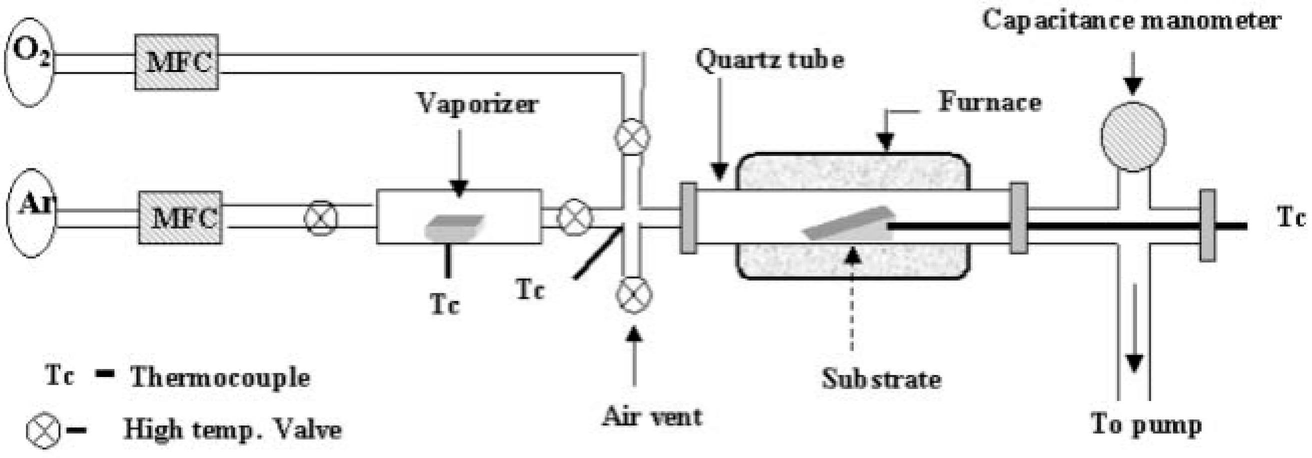

Figure 1.8 Schematic illustration of the hot-wall, low pressure CVD reactor proposed by Shivashankar.[61]

1.4 Thermal Evaporation-Like Synthesis for Vanadium Oxide NWs

Recently, we applied a facile route to control the growth of nearly aligned MoO_3 and V_2O_5 nanowires (NWs) on varies substrates based on thermal evaporation.[62-63] In the case of V_2O_5, the V_2O_5 nanowires were deposited on the surface of glass substrate as following: First, a mixture of V_2O_5 powder (0.1g, 0.55mmole) and $NH_2OH{\cdot}HCl_{(aq)}$(3M, 2mL) was placed in a glass vial stirring at 50^{o}C. After the color of mixture turned from orange to blue, a glass slide rinsed by ethanol and deionized-water was covered on the top of the glass vial. Thereafter, this installation was transferred to a programming furnace. The temperature was raised to 400°C over duration of 1 hour, and the V_2O_5 nanowires were grown on the surface of glass slide; a schematic illustration appears in Figure 1.9.

Initially, the dispersed bulk V_2O_5 powder was reduced by $NH_2OH{\cdot}HCl_{(aq)}$ to form a pre-mixture with blue color indicative of the formation of polyvanadate species (VO_x). During the thermal treatment, the polyvanadate species were transport to the surface of glass with the assistance of $H_2O_{(g)}$ and $NH_{3(g)}$ (vaporized from decomposed $NH_2OH{\cdot}HCl$). During calcination with elevated temperature, the polyvanadate species stacked and crystallized, leading to growth of NW-formed V_2O_5. The study demonstrated that the presence of $NH_2OH{\cdot}HCl$ in the growth process was found to be essential, which was not only provided the H_2O and NH_3 vapor source but also reduced V_2O_5 to polyvanadate species dissolved in solution.

Comparing with other synthetic routes (hydrothermal, sol-gel, etc.) which suffer from long reaction time and complicated cleanup procedures, and this thermal evaporation method exhibits the advantages of simple, economical, mild and time-saving treatment for preparing V_2O_5 nanowires thin film on the substrate directly. Moreover, this method is anticipated to be applied to fabricate various metal-oxide nanocrystals on oxide substrates with special crystal morphologies on choosing a suitable precursor. Owing to these features, this thermal evaporation method still possesses much potential development and is worth to continually study.

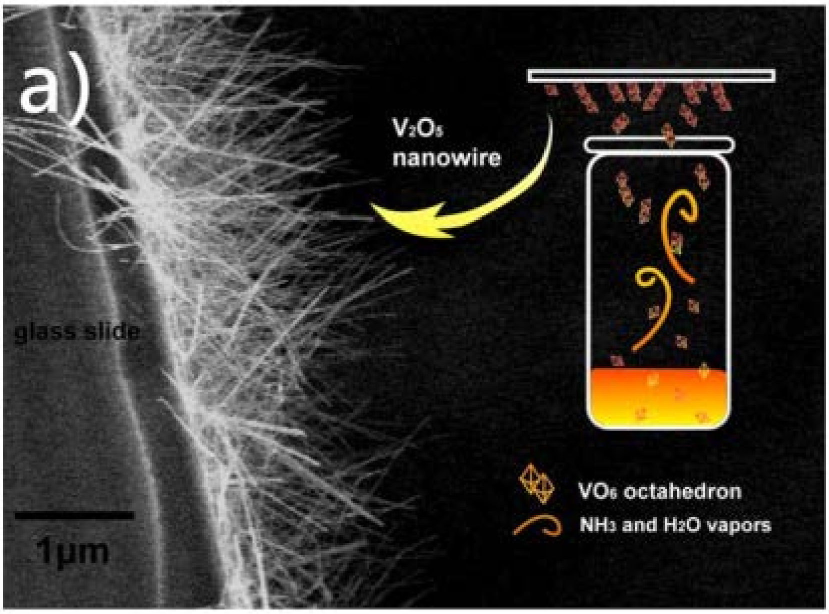

Figure 1.9 Schematic illustration of experiments to deposit V_2O_5 NWs on the surface of a substrate.[62]

1.5 Theory of Electron Field Emission

1D nanostructures, such as nanobelts, nanorods, nanotubes, and nanowires, have raised much attention in the field emission application owing to their unique electrical properties, chemical stability, and high aspect ratios in appearance of these materials. Electron field emission (EFE) is a quantum tunneling phenomenon of electron from the surface of a material subjects to a strong electron field. The energy diagram of a metal-vacuum system without external electric field is shown in Figure 1.10a. When a sufficiently high field was applied on a metal or semiconductor, electrons will tunnel through the surface potential barrier of the sample surface into vacuum level. As shown in Figure 1.10b, the vacuum level is bent and reduced at extremely high electric field. Energy barrier between the surface of metal and the vacuum become so narrow that the electron can tunnel through it easily, even at very low temperature.

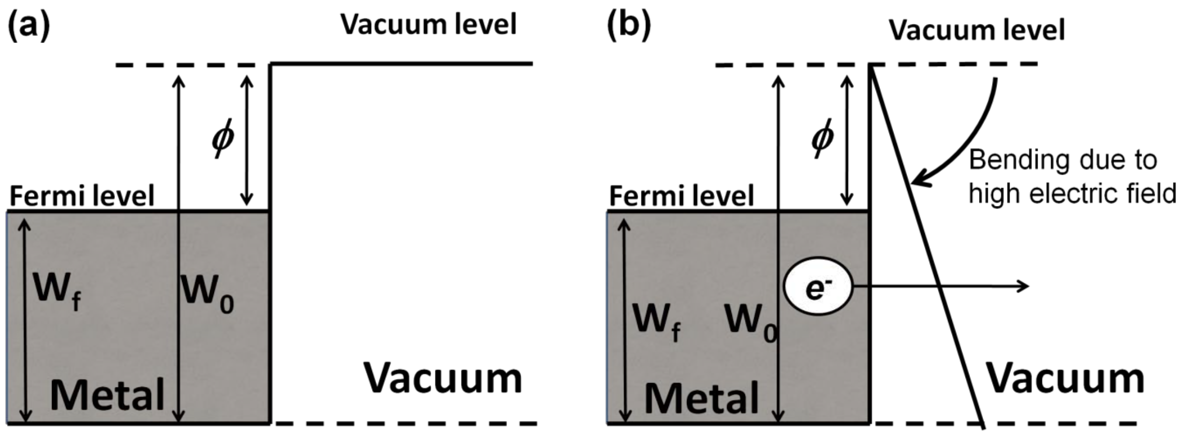

Figure 1.10 Energy diagram of metal-vacuum level (a) without electric field, (b) under high electric field.

Fowler and Nordheim obtained the accurate description of field emission, based on tunneling of electrons through the surface potential barrier, in 1928.[64] Considering the emission of electrons from a object, the emission current defined by multiplying the number of electrons N(W,T) is determined to multiply the flux of electron incident on the surface potential barrier and the tunneling probability of electrons to overcome the potential barrier as shown below.

$$J(E,T) = e\int_0^\infty N(W,T)D(W)dW \tag{1.1}$$

When E, T represent the applied electric field and the temperature, N(W,T) and D(W) are the function of E, and T. By integrating equation (1.1), it will change into

$$J(E,T) = \frac{e^3E^2}{16\pi^2 h\phi t^2(y_0)} \frac{\pi c_0 k_B T}{\sin(\pi c_0 k_B T)} \exp\left[-\frac{4}{3e}\left(\frac{2m}{h^2}\right)^{1/2} v(y_0)\frac{\phi^{3/2}}{E}\right] \tag{1.2}$$

while the time factor is

$$y_0 = 3.79\times10^{-4}\, E^{1/2}\big/\phi \tag{1.3}$$

The velocity is

$$V(y_0) \tag{1.4}$$

Set T approximate to zero to discuss the field emission, equation (1.2) could be shown as

$$J(F) = AF^2 \exp\left[\frac{-B\phi^{3/2}}{F}\right] \tag{1.5}$$

while $A \equiv \frac{e^3}{16\pi\hbar\phi t^2(y_0)}$, and $B \equiv \frac{4}{3e}\left(\frac{2m}{\hbar^2}\right)^{1/2} v(y_0)$

This is known as Fowler-Nordheim equation. Under the field emission condition, y is between 0-1, and the function of $v(y)$ and $t^2(y)$ could be approximated to:

$$t^2(y) = 1.1\,,\ v(y) = 0.95 - y^2$$

By substituting the approximation above, J = I/α, and F = βV into equation (1.5), the expression becomes

$$I = aV^2 exp\left(\frac{-b}{V}\right) \tag{1.6}$$

where $a = \frac{\alpha A \beta^2}{1.1\phi} \exp\left[\frac{B(1.44\times10^{-7})}{\phi^{1/2}}\right]$ and $b = \frac{0.95B\phi^{3/2}}{\beta}$

$A = 1.54\times10^{-6}$, $B = 6.87\times10^{-7}$.

A denotes the effective emission area and β is the field enhancement factor. There are three factors, α, β, and ϕ, in equation (1.6) could influence the magnitude of the field emission current density. equation (1.6) can be further expressed as

$$\ln\left(\frac{I}{V^2}\right) = \ln a - b\left(\frac{1}{V}\right) \tag{1.7}$$

As a consequence, for a field emission data, by plotting of log(I/V^2) versus 1/V, a straight line with negative slope could be obtained, and was designated as F-N plot. Through this plot, one can judge the field emission properties of a sample. When the work function of the sample is known, the field enhancement factor could be calculated from the slope of F-N plot.

Table 1.2 FE parameters of 1D nanostructures in the previous study

Emitters	Synthesis method	E_{to}(V/μm)[a]	J_{max} (mA/cm^2)[b]	β	ref
V_2O_5 nanowires	Thermal evaporation	8.3	1.6 at field of 18 (V/um)		62
V_2O_5 nanotubes	Template-based wetting	7.3	2.1 at field of 9.0 (V/um)		3
V_2O_5 nanorods	Template-based wetting	6.4	2.31 at field of 9.2 (V/um)		4
V_2O_5 nanowires	Hydrothermal	2.8	14.7 at field of 4.42 (V/um)	2256	36
ZnO nanotubes	CVD	7.3	1.3 at field of 11.8 (V/um)		65
ZnO nanoneedles	CVD	2.5	-	2000	66
MoO_3 nanowires		3.5	13 at field of 8.0 (V/um)		67
MoO_3 nanoflowers	CVD	8.7	-	-	68
SnO_2 nanowires	CVD	4.03	-	1008	69
Ga_2O_3 nanowires	CVD	6.2	-	880	70
WO_3 nanowires	CVD	4.45	-	-	71
WO_3 nanowires	CVD	4.0	2.25 at field of 7.0 (V/um)	1904	72

a: E_{to}: turn-on field b: J_{max}: maximum current density

1.6 Aim of This Thesis

Vanadium oxides and their derivatives exhibit outstanding chemical and physical properties, which are used in many fields. A facile and economical way to grow vanadium oxides NWs represents a significant improvement for application in future nanodevices. The conventional synthetic routes suffer from time-consuming, complicated procedure, and uneconomic. Previously, our group reported a facile route to control the growth of nearly aligned V_2O_5 and MoO_3 nanowires on varies substrates based on thermal evaporation. It is anticipated that the synthetic procedure is suitable for preparing other 1D metal oxides.

In this thesis, we extend this deposition process to obtain binary and ternary phase of vanadium oxides with 1D nanostructure. We tried to combine the original thermal evaporation procedure with post-reduction treatment to obtain reduced vanadium oxide. In the first part, V_2O_5 NWs thin-films were first deposited on the surfaces of substrates via a thermal evaporation route. The reduced vanadium oxide phase of VO_2 and V_2O_3 NWs were obtained by adjusting the experimental parameters of reduction. In the second part, the target product we planned to prepare is β-$Na_xV_2O_5$, and a well–controlled Na^+ ion source is necessary. Based on this concept, a modified thermal evaporation with an surface pre-treatment of substrate was developed. The sodium silicate is used as the source of the sodium ion, which was first coated on the substrates and the amount of precursor was carefully controlled on a Na^+-free substrate. The polyvanadate species are delivered to the surface of substrate during evaporation process, which were further react with Na^+ ion to form a ternary compound of β-$Na_xV_2O_5$.

Several analytical techniques were used to confirm the nature of as-prepared typical product, and the crystalline, morphology, reaction condition, and growth mechanism of these nanowires and thin-film would be discussed in detail. Finally, field emission properties of these NWs sample are demonstrated and studied in this work.

Chapter 2.

Controlled Reduction of Nearly-Aligned Nanowires of V_2O_5 to VO_2(R), VO_2(B) and V_2O_3

2.1 Introduction

In the previous section, we mentioned a facile route to control the growth of nearly aligned MoO_3 and V_2O_5 NWs on varies substrates. The as-synthesized V_2O_5 NWs on substrate were further used as a precursor to prepare reduced vanadium oxide nanowires with controlled reduction conductions. In this section, we had set a systematic reduction condition and successfully obtained several reducing vanadium oxide phase of VO_2(R), VO_2(B), and V_2O_3 by adjusting reaction period or the composition reducing gas flow. The structural information of reducing vanadium oxide nanowires was investigated with various analytic techniques such as SEM, TEM, SAED, XRD, and XPS. In addition, field emission measurements were carried out and the results show small actuation voltages and a large current density of reducing vanadium oxides NWs arrays, which properties are prospectively useful in optoelectronic nanodevices.

2.2 Experimental

2.2.1 Synthesis

2.2.1.1 The V_2O_5 nanowires film

V_2O_5 nanowires were grown on a substrate with a thermal evaporation method developed in previous study. The details of the deposition procedures are described elsewhere.

2.2.1.2 The Reduction of the Nanowires Thin Film

Before reduction reaction, V_2O_5 NWs were examined with P-XRD to check the purity. Initially, pure V_2O_5 nanowires thin film was placed in an alumina crucible, which was subsequently placed in a tube furnace. The reduction reaction proceeded with constant heating rate 200^{o}C hr^{-1} and kept at the 450°C. The vanadium oxide nanowires with different oxidation states were obtained by adjusting the composition of the reducing gas and the reaction period, and the parameters were summarized in Table 2.1.

Table 2.1 Parameter of reduction reaction and refined cell parameter of as-obtained reduced product

	Parameter of reduction			Refined cell parameter					
Product	composition	Temp.	duration	lattice	Space group	a(Å)	b(Å)	c(Å)	β(°)
VO_2(R)	10%H_2/90%Ar	450°C	12 hours	monoclinic	$P2_1/c$	5.74	4.53	5.38	122.65
VO_2(B)	100% H_2	450°C	2 hours	monoclinic	C2/m	12.03	3.69	6.39	106.88
V_2O_3	100% H_2	450°C	4 hours	hexagonal	R-3c	4.94	4.94	13.99	-

2.2.2 Characterization

The crystalline were measured by powder X-ray diffraction (XRD, Bruker AXS D8 Advance, Leipzig Germany) with Cu-Kα radiation operating at 40kV, 40 mA. The micrographs of scanning electron microscope (SEM, Hitachi, S-4700I, operated at 15kV) and transmission electron microscope (TEM, JEOL, JEM-3000F, operated at 200kV) were used to determine the morphology and the size of nanowires. The samples for TEM experimental were prepared as-following: first, the NWs were separated from glass by ultrasonic dispersion of the thin film in ethanol for 5 minutes. Then, the dispersion solution was dropped onto a copper grid (carbon film-coated 100 mesh), and dried in air atmosphere leaving spread NWs on the carbon film. X-Ray photoelectron spectroscopic analysis was made with a XPS spectrometer (PHI Quantera SXM); the binding energy was calibrated by use of the C-1s line at 284.4eV. For field emission measurement, the vanadium oxide thin films were placed into a vacuum chamber with a pressure less than 3×10^{-7} Pa at room temperature. The distance between the electrode and sample was fixed at 100μm and the high-voltage sourcemeter (Keithly 2410) was used to measure the current-to-voltage characteristics.

2.3 Results and Discussion

2.3.1 Synthesis and Reduction Condition

To prepare vanadium oxides NWs thin film with various oxidation states, the as-prepared V_2O_5 NWs were heated in a tube furnace under H_2/Ar pre-mixed gas with specific composition and flow rate of 0.4 SLPM (Standard Liter Per Minute). The initial attempt to reduce V_2O_5 thin film was carried out under ambient concentration of H_2/Ar pre-mixed gas. It was found out that the VO_2(R) and VO_2(B) can be synthesized with low and high concentration of H_2, separately. On the basis of this finding, we set two reduction systems to control the product of reduced vanadium oxide. All parameters and results of the reduction condition are referred in Table 2.2, and the pure phase of reduced vanadium oxides were obtained according to the condition presented in Table 2.1.

Table 2.2 Parameter and final product of two reduction system

	System	temperature	composition	duration	product
1	Mild	450°C	10%H_2	6hr	V_2O_5
2	Reduction	450°C	10%H_2	9hr	V_2O_5+VO_2(R)
3	System	450°C	10%H_2	12hr	VO_2(R)
4	Rapid	450°C	100%H_2	2hr	VO_2(B)
5	Reduction	450°C	100%H_2	4hr	V_2O_3
5	System	450°C	100%H_2	6hr	V_2O_3

2.3.2 Structural and Purity Characterization

The crystallinity and purity of as-prepared NWs were confirmed by using powder XRD, as shown in Figure 2.1. The XRD profile of for V_2O_5 NWs can be indexed as orthorhombic unit cell (JCPDS number: 72-0589, space group: $Pmn2_1$; a = 11.45 (2) Å, b = 4.430 (6) Å, c = 3.542 (3) Å). Figure 2.1b shows the XRD pattern of reducing product obtained at mild reduction condition (condition 1), which corresponds to monoclinic rutile VO_2 (JCPDS number, space group :43-1051) On the other hand, rapid reducing conditions (condition 2 and 3) preferred to form VO_2-B (Figure 2.1c, JCPDS number: 65-7960) and V_2O_3 phases (Figure 2.1d, JCPDS number: 84-0316). Refined lattice parameter of all reducing product were referred in Table 2.1. The XRD profile of VO_2(R) and VO_2(B) show low signal-to-noise ratios for all diffraction peaks, indicative of low yield and the formation of amorphous phase. According to these results, we assume that the reduction reaction can be regarded as continuous process, and the vanadium oxide will be reduced continually by hydrogen. The transformation of V^{4+} into V^{3+} occurs immediately after the conversion of V^{5+} to V^{4+}. V^{4+} can be defined as the transition state during the reduction reaction and we limit the duration time to cease the reaction and preserve the vanadium oxide with V^{4+} state. Furthermore, the amorphous VO_x (oxidation states of V and III) are also preserved at the same time and PXRD profiles reveal a low signal-to-noise ratio. The lowest oxidation state of vanadium ion is +3 in V_2O_3. When the duration time of reduction was increased, the amorphous VO_x species would be completely converted to V_2O_3 and crystallize, which results in a PXRD pattern with good signal-to-noise ratio.

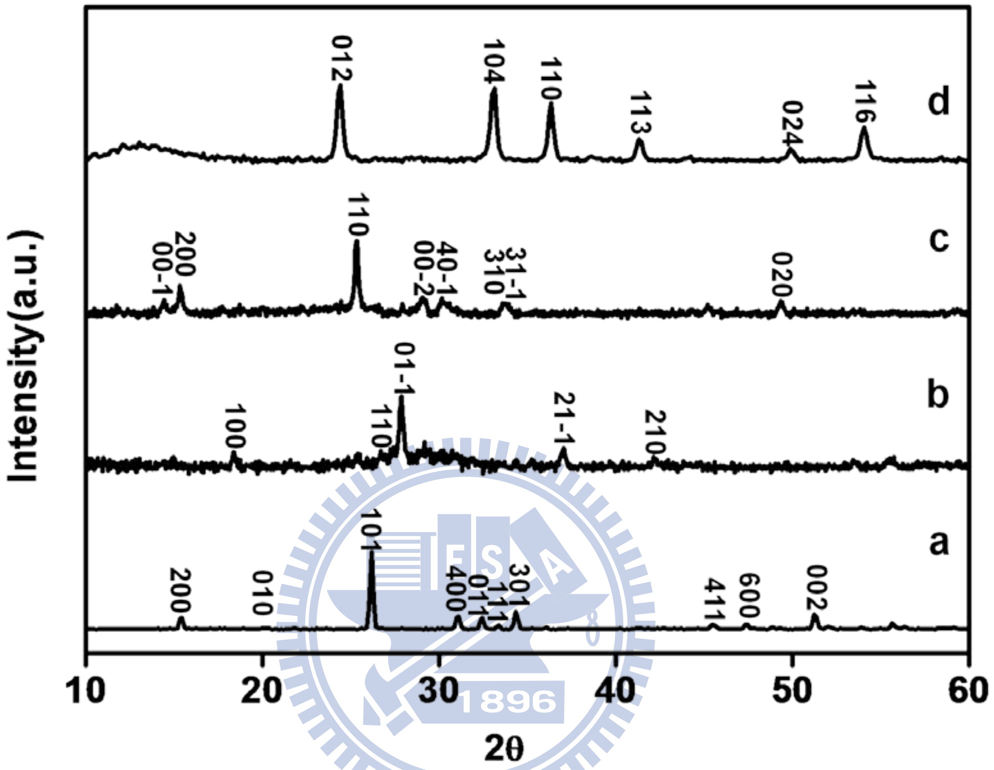

Figure 2.1 the XRD profiles of (a) V_2O_5, (b) VO_2(R), (c) VO_2(B) and (d) V_2O_3.

2.3.3 The Morphology and Structure of As-Obtained Typical Product

The representative morphology and structure of as-prepared NWs were investigated by FE SEM and TEM, as shown in Figure 2.2 and Figure 2.3, respectively. Figure 2.2a shows the SEM image of V_2O_5 NWs, and the microstructures of that are long uniform nanowires. Large portion of V_2O_5 NWs possesses length of up to tens of micrometer as calculated from SEM image. Other SEM image (see Figure 2.4) also confirm the NWs structure of V_2O_5 with width of 70~150nm. The side view image (inset of Figure 2.2a) clearly reveals that V_2O_5 NWs are nearly vertical-aligned to the surface of the glass. Figure 2.2b-2.2d show the SEM images of the reduced product, and the insets are their corresponding side view image. The results suggest that the large portions of NWs microstructure are maintained with nearly vertical-aligned structure to the surface. It is demonstrated that the morphology is not destroyed during the reduction reaction.

Figure 2.3a shows the TEM image of a single V_2O_5 NW and insets show its corresponding selected area electronic diffraction (SAED) pattern (top) and high resolution-TEM (HR-TEM) image (bottom). The SAED pattern and HRTEM image of a single wire recorded from [0 1 0] zone axis, and SAED pattern reveals sharp and clean diffraction spots, indicative of single crystalline property. HRTEM image indicates lattice fringe of 5.72Å and 3.39Å, corresponding to (2 0 0) and (1 0 -1) crystal planes for orthorhombic V_2O_5, respectively. The growth direction is along the c-axis, which is deduced from the angle of 90° between the c-axis and the a axis, consistent with the previous studies. Figure 2.3b-2.3d show the TEM images of single NW of reduced products and insets show their corresponding SAED pattern (top) and HR-TEM image (bottom). The SAED pattern and HR-TEM of VO_2(R), VO_2(B), and V_2O_3 single wire were recorded from zone axis of [2 -1 1], [0 0 1], and [2 -2 1], respectively. All SAED pattern of reduced product also exhibits sharp and clean diffraction spots owing to single crystalline property. The HR-TEM taken of a portion of VO_2-R NWs reveals parallel lattice fringes with inter-layer distance ~3.31 Å and 3.19 Å, which corresponding to plane (1 1 -1) and (0 1 1). Combined with the TEM image, the growth direction of VO_2(R) NW is closed to the vector which is perpendicular to the plane (1 1 -1). The HR-TEM of VO_2(B) NWs shows the d-spacing of 3.5 Å and 5.7 Å, consistent with that of the (1 -1 0) and (2 0 0), respective. The growth direction of VO_2(B) NW is along the b-axis, which is deduced from the angle of 90° between the b-axis and the a axis. As shown in Figure 2.3d, the marked interplanar d-spacing of 2.5 Å and 5.0 Å corresponds to the (0 1 -2) and (1 -1 4) lattice plane of hexagonal V_2O_3. The results of SAED and HR-TEM demonstrate that the V_2O_3 NWs are single crystalline in structure along growth direction of the normal vector of plane (1 1 0), which can be deduced by using the angle of 90° between two normal vector of plane (1 1 0) and (1 -1 4). The crystal growth directions of all reduced products are suggested by SAED and HR-TEM analyses, and that is influenced by the conversion of precursor product V_2O_5 NWs.

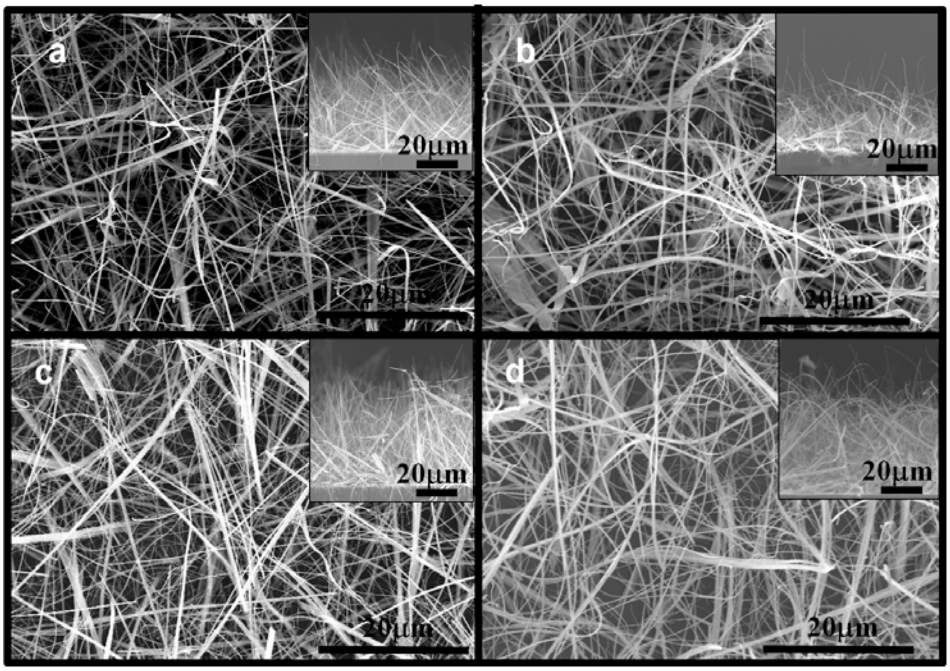

Figure 2.2 Top view SEM image and corresponding side view image (inset) of (a) V_2O_5, (b) VO_2(R), (c) VO_2(B), (d) V_2O_3 NWs thin-film.

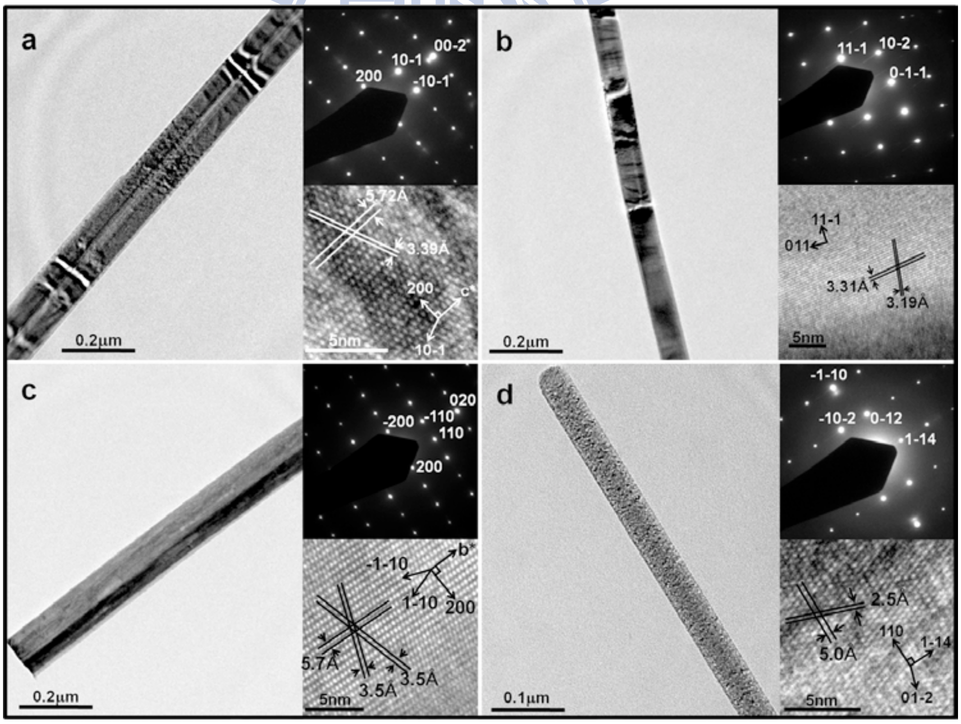

Figure 2.3 TEM (left), SAED (right top), and HRTEM (right bottom) images of as-obtained (a) V_2O_5, (b) VO_2(R), (c) VO_2(B), (d) V_2O_3 NWs, respectively.

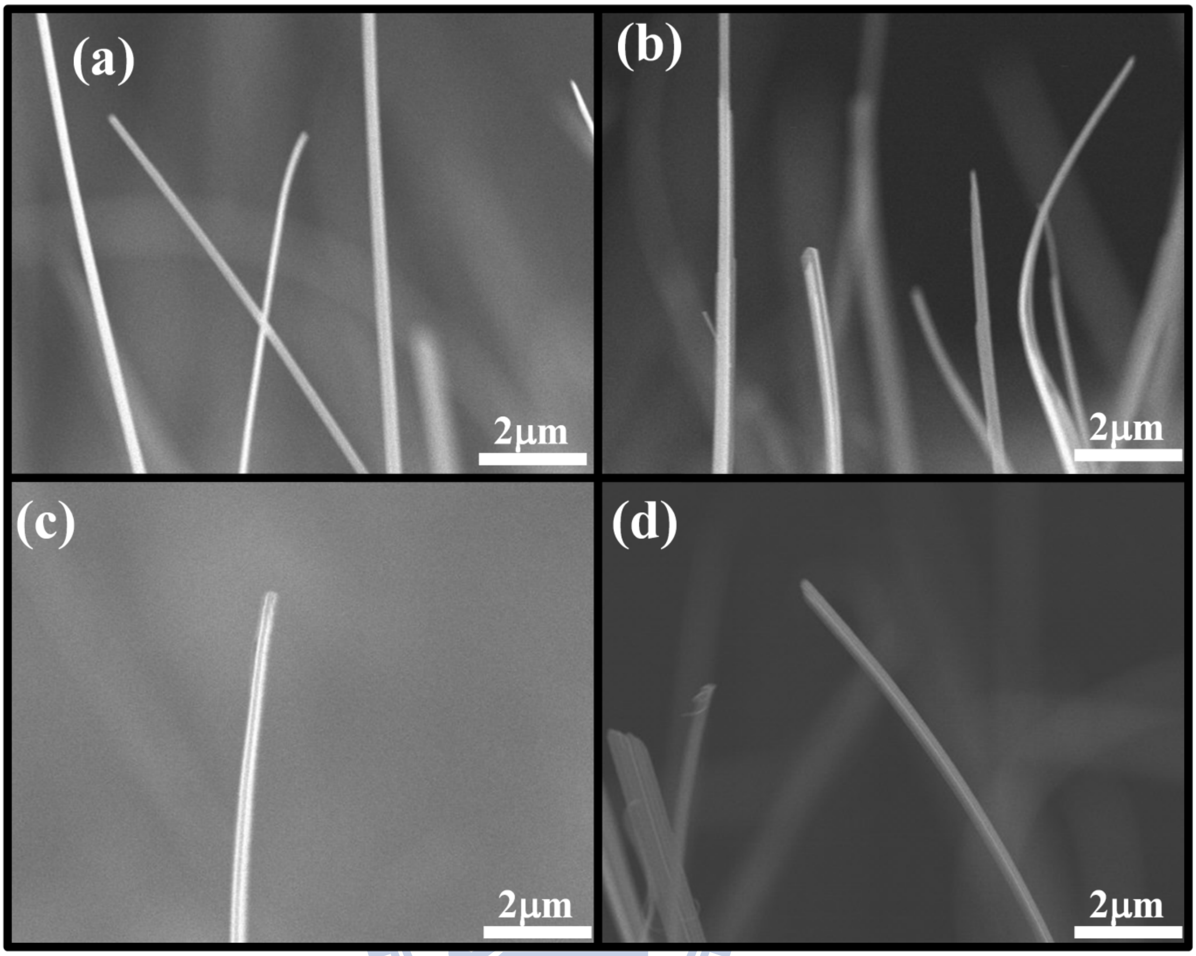

Figure 2.4 High magnitude resolution of side view image of as-prepared (a) V_2O_5, (b) VO_2(R), (c) VO_2(B), (d) V_2O_3 NWs

2.3.4 X-Ray Photoelectron Spectroscopic Analyses.

XPS analyses have been further achieved to investigate the information of the oxidation state of vanadium ions in as-prepared product. As shown in Figure 2.5, the high resolution XPS spectra for V 2p region shows the binding energy of V $2p_{1/2}$ and V $2p_{3/2}$. The peak in V $2p_{3/2}$ spectrum of VO_2R and VO_2B (Figure 2.5b and 2.5c) are broad ranging from 514 eV to 518 eV, indicative of mixed oxidation states of vanadium ion. After peak modeling, the V $2p_{3/2}$ spectrum contains three contributions at 517.02 eV, 515.93 eV, and 515.04 eV corresponding to V^{5+}, V^{4+}, and V^{3+} ions. These results demonstrate that amorphous phase of V^{3+} and V^{5+} complex certainly exist in VO_2-R and VO_2-B and result in low signal-to-noise ratio in XRD pattern. The broad peak caused by mixed oxidation states of vanadium ions (V^{5+}, V^{4+}, and V^{3+} ions) can also be found in the V $2p_{3/2}$ spectrum of V_2O_3 (see Figure 2.5d). The appearance of V^{5+} and V^{4+} ions might be due to the oxidation of vanadium ions at the surface of NWs, and this phenomenon are over-amplified by XPS owing to its surface sensitivity. In our case, the amount of oxidation vanadium ions existing at the surface of the NWs are too less to measure at XRD.

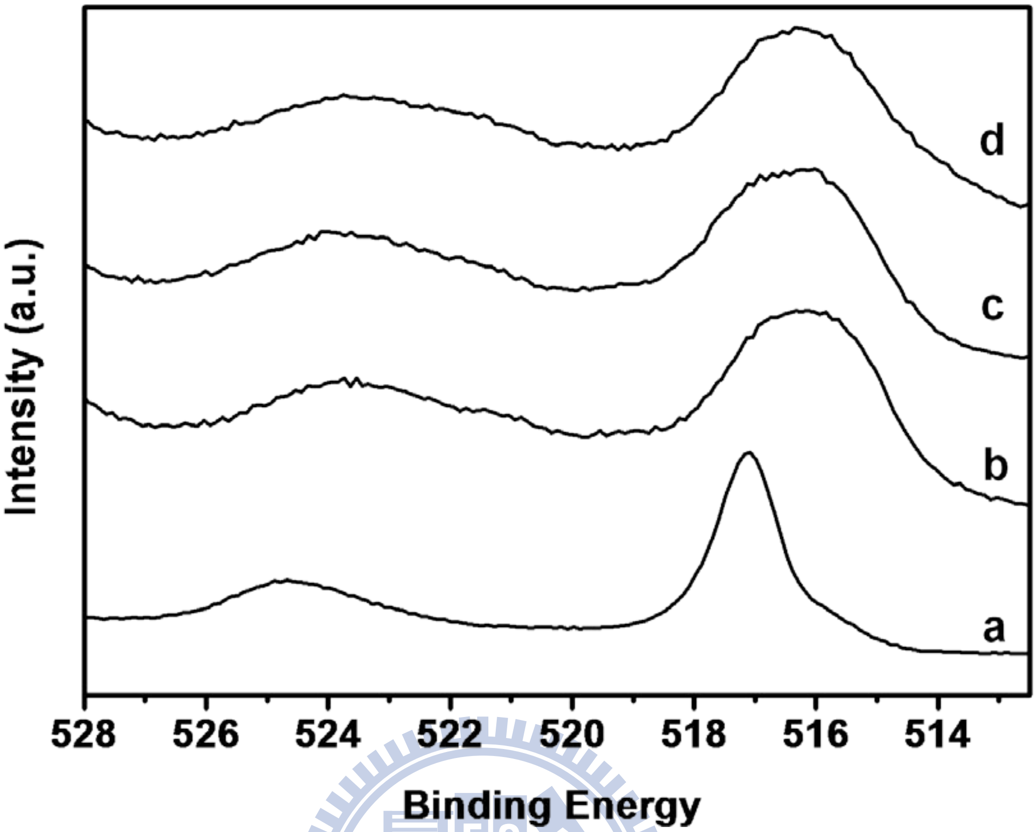

Figure 2.5 XPS spectrum for V-2p region of as-prepared (a) V_2O_5, (b) VO_2(R), (c) VO_2(B), (d) V_2O_3 NWs thin film, respectively.

2.3.5 Transformation Mechanism

To realize the transformation mechanism, we assume that the crystal growth directions of all reduced products are influenced by the precursor product V_2O_5 NWs. Based on this assumption; we proposed the schematic illustration of transformative evolution according to the growth direction of each phase of VO_x NW. The Figure 2.6 shows the single atomic layers of each phase of VO_x NW along with their corresponding growth plane, which were determined from the crystalline analyses of HR-TEM and SAED. The Figure 2.6a shows one layer of (001) plane for V_2O_5 structure, and the layer structures along b-axis are the key fragment structure for the transformative evolution. During reduction treatment with reducing gas, the distance of each adjacent layer will become close and the layers will connect with each other through the O-V-O bond to form 3D network structure. The lowest oxidation state of vanadium ion is +3 in V_2O_3, and two intermediates can be found in VO_2(R) and VO_2(B) phases. It is considered as a continuous process, the transformation from V_2O_5 to VO_2 (route a and b) will occur first, then VO_2 phase will further convert into V_2O_3 (route c and d).

In route a, the odd layer of V_2O_5 fragment will be shifted with respective original location by -1/4, -1/2, 0. After the dislocation, the odd layers will connect with even layers by dangling oxygen atoms and the redundant oxygen atoms will be removed by hydrogen molecules. The formative layer structures will close to adjacent one and further form a new bonding between vanadium and oxygen atoms, resulting in VO_2(B) phase structure.

In route c, the VO_2(B) phase will further be reduced to form V_2O_3 phase. When the reduction treatment is kept going, VO_2(B) will undergo the similar process with route e. The fragments of VO_2(B) will shift along a-axis and connect with adjacent one through originally dangling oxygen atoms. Also, the redundant oxygen atoms will be removed by hydrogen molecules to form the final V_2O_3 structure.

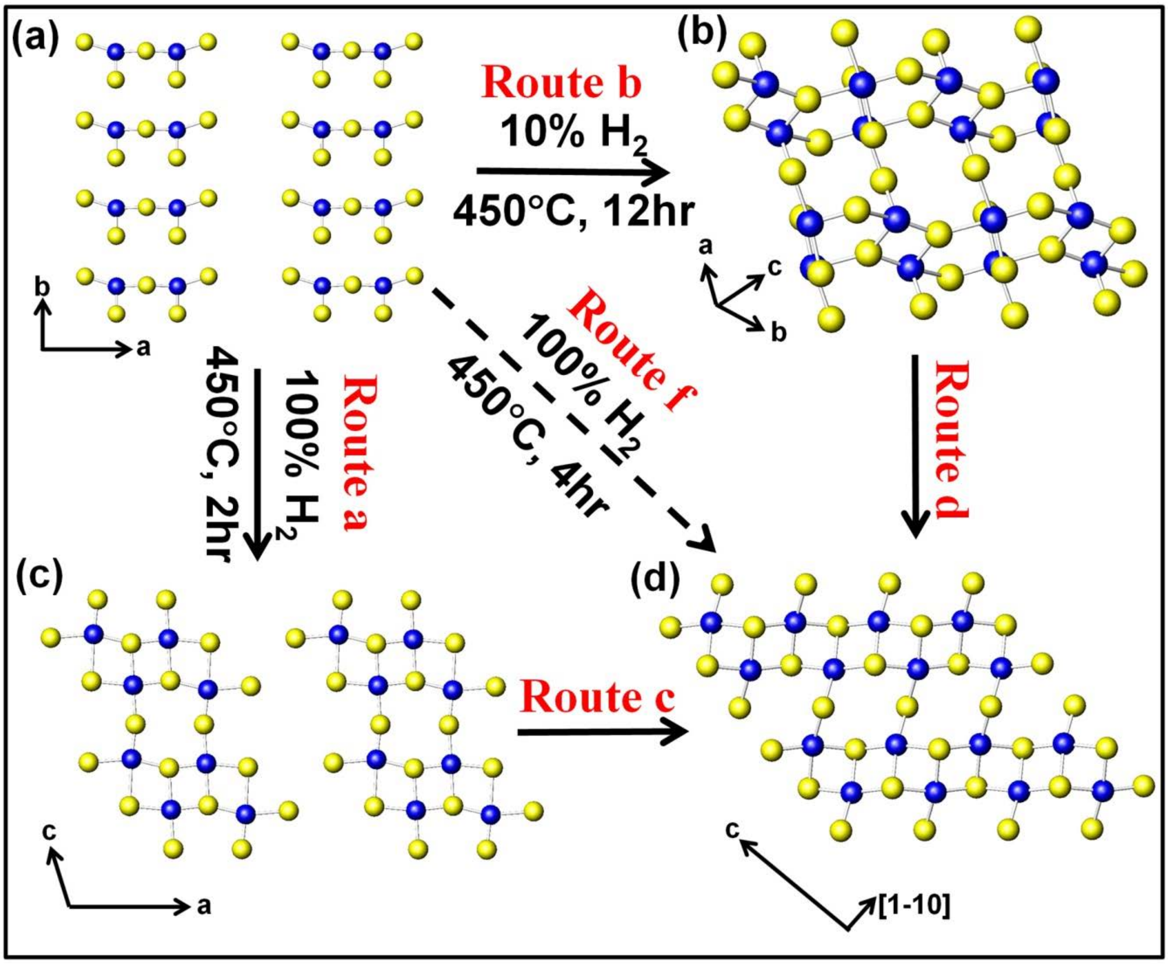

Figure 2.6 Schematic illustration of transformative evolution. It shows single atom layers of (a) V_2O_5, (b) VO_2(R), (c) VO_2(B), (d) V_2O_3 along their corresponding growth plane.

2.3.6 Electronic Field Emission Property.

The interesting electronic field emission properties of as-prepared typical product were measured in a vacuum box with a parallel-plate configuration of electrodes with a separation 100μm between the anode and an emitting surface of area $0.785mm^2$. Figure 2.7 reveals the emission current density (J) versus an applied macroscopic field (E) within a ~0-1100V bias voltage range at separations of 100μm between the samples and electrode. The turn-on field (E_{to}), defined as the macroscopic field required producing a current density of $10\mu A/cm^2$, and the maximum current density (J_{max}) are summarized at Table 2.3. The un-reduced V_2O_5 NWs thin film possesses the poor FE properties with E_{to} of 8.3 V/μm and J_{max} of $3.68\ mA/cm^2$ at the field of 11V/um. The results reveal that the FE properties are improved obviously when the V_2O_5 NWs convert to other reduced vanadium oxide. Notably, the FE properties are effective to be improved as oxidation state decreasing. Among these typical product, the lowest oxidation state V_2O_3 NWs exhibit the best FE properties with E_{to} of 5.2 V/μm and J_{max} of $8.3\ mA/cm^2$ at the field of 8.3V/um. The variations of the turn-on fields may be attributed to the differences in phases and chemical compositions. A Fowler–Nordheim (F–N) plot of (ln I/E2) versus (1/E) appears in the inset of Figure 2.7; a linear relation indicates that the field emission from the films of all vanadium oxides NWs agrees with the F–N theory and the emitted currents are produced owing to quantum tunneling at the surface.

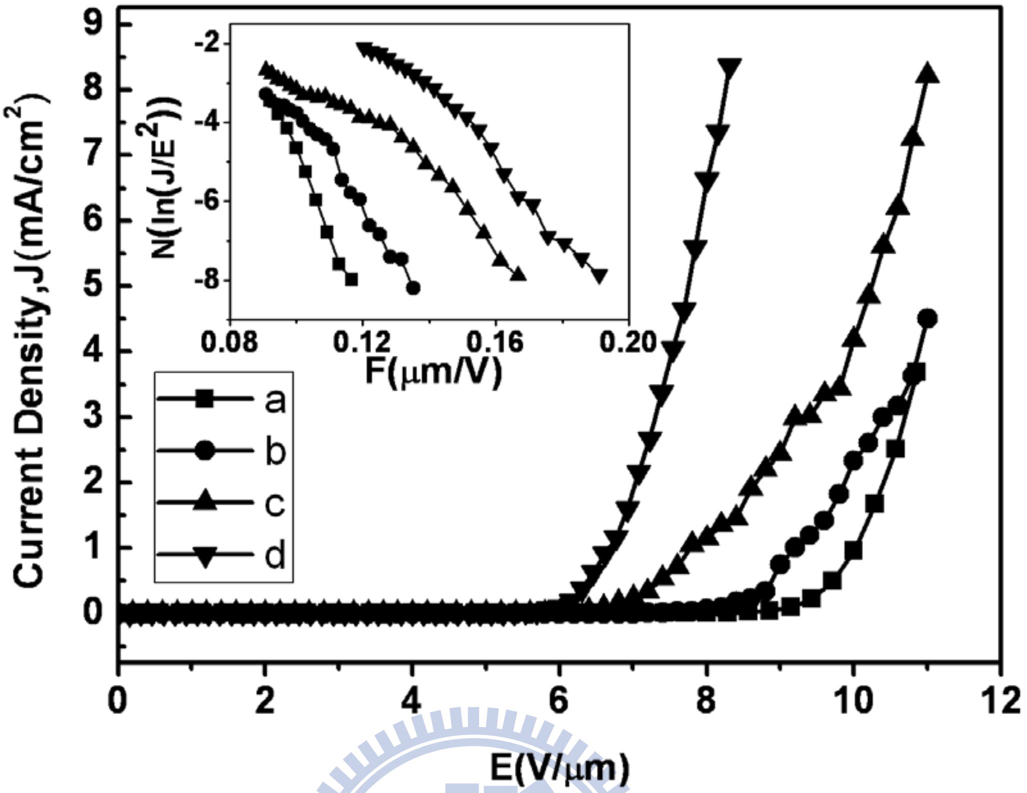

Figure 2.7. The plot of Field emission current density verse applied electric field and its corresponding Fowler-Nordheim plots (inset) of as-prepared (a) V_2O_5, (b) VO_2(R), (c) VO_2(B), (d) V_2O_3 NWs thin-film, respectively.

Table 2.3 FE properties as-prepared product NWs

	E_{to}(V/μm)	I_{max}(mA/cm^2)
V_2O_5 NWs	8.3	3.68 at an applied field of 11V/μm
VO_2(R) NWs	7.2	4.50 at an applied field of 11V/μm
VO_2(B) NWs	6.0	8.21 at an applied field of 11V/μm
V_2O_3 NWs	5.2	8.36 at an applied field of 8.3V/μm

2.4 Summary

In this section, we reported the synthesis of nearly aligned VO_x NWs with precursor of V_2O_5 NWs on substrate. Products of VO_2(R), VO_2(B), and V_2O_3 NWs were successfully obtained via controlled concentration of reducing gas flow and reduced period. We also demonstrate the single crystalline properties of reduced vanadium oxides NWs with specific growth direction. On the basis of the growth direction of each product, possible mechanisms of conversion during reduction reaction are proposed. All as-obtained VO_x NWs possess interesting field emission properties with linear F-N property, which are influenced by morphology of NWs and the nature of material. Among these NWs, V_2O_3 NWS shows the best FE properties with a low turn-on field of 5.3 V/μm and a maximum current density of 8.3 mA/cm^2 at the applied field of 11.0 V/μm. The feature of vanadium oxide shows excellent FE properties with low turn field and high maximum current density, which might be used as field emission emitter.

Chapter 3

Controlled Synthesis of Nearly Vertical-Aligned $Na_{0.24}V_2O_5$ Nanowire Thin Films

---

3.1 Introduction

As a member of vanadium oxide derivative compounds, β-$Na_xV_2O_5$ (x=0.23-0.41) have been synthesized with 1D nanostructure by CVD and hydrothermal route, which require long reaction time and complicated procedures.[51-52, 58, 60] Moreover, grown NWs of $Na_{1+x}V_3O_8$ and β-$Na_xV_2O_5$ on glass substrates were reported.[60, 73] The source of Na^+ ions was from the substrate that diffused into the vanadium oxide precursor.

In this section, a ternary phase of bronze vanadium oxide β-$Na_xV_2O_5$ NWs were successfully deposited on the substrate via a modified procedure that combined the original procedures with an additional treatment on the surface of substrate. The source of the Na^+ is from sodium silicate, which was first coated on the substrates and the amount of precursor was carefully controlled. Several parameters, including reaction temperature and the concentration of reactants, were found to play important roles in controlling morphology of the final products. Field emission measurements were carried out and the results show small actuation voltages and a large current density of β-$Na_xV_2O_5$ NWs arrays, which properties are prospectively useful in an optoelectronic nanodevice.

3.2 Experimental Section

3.2.1 Synthesis

Thin films of β-$Na_xV_2O_5$ NWs were grown on a substrate with a two-steps synthetic process including substrate treatment and thermal evaporation.

3.2.1.1 Substrate treatment.

Sodium metasilicate solutions (Na-solution) were prepared by dissolving Sodium metasilicate ($Na_2SiO_3 \cdot 9H_2O$) in deionized water with concentrations ranging from 0.0125M to 0.05M. Prior to the coating treatment, a sodium-free glass substrate (2cm×1cm) was first cleaned by ethanol and deionized water, followed by dropping 0.2 ml of as-prepared solution onto substrate, and finally dried overnight at 40°C to form a thin film of sodium metasilicate salt on the glass.

3.2.1.2. Thermal evaporation.

The solution for each precursor was prepared as following: V_2O_5 powder (0.1g, 0.55mmole) and $NH_2OH{\cdot}HCl_{(aq)}$(3M, 2mL) were well mixed in a glass vial, and stirred at 50°C. The concentration of precursor solution was ranged from 0.15M to 0.45M with fixed ratio of V_2O_5 and $NH_2OH{\cdot}HCl$. The color of mixture finally turned from orange to blue, indicating the reduction of V_2O_5. Thereafter, a glass substrate as prepared was placed on the top of the vial, and this installation was transferred into a programming furnace. The temperature was raised to 300°C -400°C with a constant rate of 100°C /hr and kept for 1 hour. Finally, well-aligned β-Na$_x$V$_2$O$_5$ NWs could be found on the lower side of glass.

3.2.2 Characterization.

The as-prepared thin film products were characterized with several analytical techniques. The crystallinity of products were confirmed by powder X-ray diffraction (XRD, Bruker AXS D8 Advance, Leipzig Germany) with Cu-Kα radiation (λ = 1.54060 Å) operating at 40kV, 40 mA. Cell parameters were refined with the program CELREF.[74] Chemical composition of the β-Na$_x$V$_2$O$_5$ NWs was determined with an inductively coupled plasma-atomic emission spectrometer (ICP-AES, Jarrell-Ash ICAP 9000). The crystal morphology and dimension of NWs were determined from the micrograph analyses of scanning electron microscope (SEM, Hitachi, S-4700I, operated at 15kV) and transmission electron microscope (TEM, JEOL, JEM-3000F, operated at 200kV). To prepare the sample for TEM experiment, the β-Na$_x$V$_2$O$_5$ NWs were scraped from glass by ultrasonic dispersion of the thin-film in ethanol for 5 minutes. The resulting solution was then dropped onto a copper grid (holey carbon-coated 100 mesh), and dried in air to spread NWs on the carbon film. X-ray photoelectron spectroscopic (XPS) analysis was made with a PHI Quantera SXM spectrometer; the binding energy was calibrated by use of the C-1s line at 284.4eV. Diffuse reflectance measurements were performed near 25°C with a UV–visible spectrophotometer (Hitachi/U-3010) and an integrating sphere was used to measure the diffuse reflectance spectra over a range 400–800 nm. For field emission measurement, the β-$Na_xV_2O_5$ thin films were placed in a vacuum chamber with a pressure less than 5×10^{-6} Pa at room temperature. The distance between the sample and electrode was adjusted to 100μm and the current-to-voltage characteristics were recorded by high-voltage source meter (Keithly 2410).

3.3 Results and Discussion

3.3.1 Structural and Composition Characterization

The crystallinity and purity of as-prepared β-$Na_xV_2O_5$ NWs were confirmed by using powder XRD. Figure 3.1 shows XRD patterns of products as deposited on a glass substrate synthesized at various temperature. The patterns can be indexed on the basis of a monoclinic unit cell with refined lattice parameters of a = 15.40 (3) Å, b = 3.612 (3) Å, c = 10.05 (3) Å, β = 109.5° (2), which is close to the calculated XRD pattern for $Na_{0.76}V_6O_{15}$ (JCPDS number: 75-1653, space group: C2/m(12)). As shown in Figure 3.1, the sample synthesized at lower temperature exhibits broad XRD signal, indicative of poor crystallinity. With raising reaction temperature, sharp XRD signal with high signal-to-noise ratio are observed due to improved crystallinity. Moreover, reaction temperature also affects the intensity of Bragg peaks. For the sample prepared at 400°C, the strongest Bragg peak set is located at (1 1 -1), whereas the samples prepared at low temperature exhibit the same maximum diffraction peak (2 0 0) as the calculated pattern. The results indicate that $Na_xV_2O_5$ NWs synthesized at 400°C exhibit preferential orientation with (1 1 -1) facet. No obvious preferential orientation is observed for samples synthesized at lower temperature. According to these results, we speculate that the NWs observed at $T < 400°C$ were randomly oriented on the substrate without any preferential orientation. This assumption will be demonstrated from cross-section view of SEM images in later section.

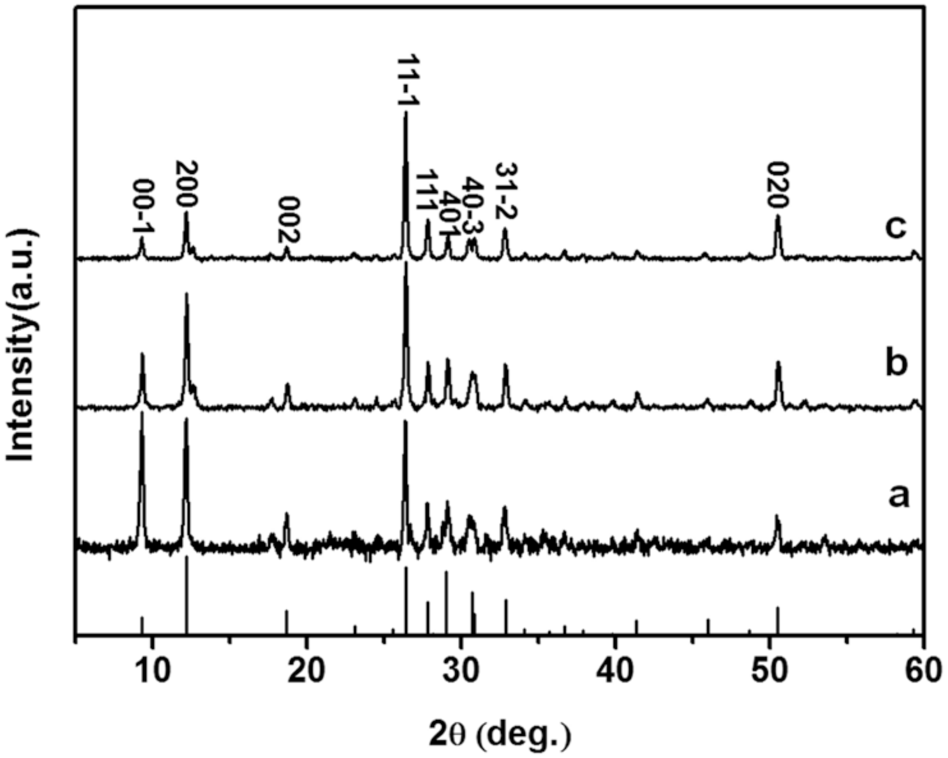

Figure 3.1 The calculated XRD pattern and the XRD profiles of typical product synthesized at the temperature of (a) 300°C, (b) 350°C and (c) 400°C.

Chemical composition of typical product was examined with ICP-AES, which shows atomic ratio of Na/V ~ 0.12. Combining with XRD result, it is concluded that the NWs deposited on the substrate via a thermal evaporation route are β phase $Na_{0.24}V_2O_5$.

3.3.2 The Morphology and Structure of As-Obtained Monoclinic $Na_{0.24}V_2O_5$ NWs

The size and morphology of the $Na_{0.24}V_2O_5$ NWs as synthesized were first examined with SEM and TEM, as shown in Figure 3.2a and Figure 3.2b, respectively. It is clear that the $Na_{0.24}V_2O_5$ product contains long and uniform NWs with average length of 35μm micrometers. Furthermore, the side view (inset of Figure 3.2a) reveals nearly vertically aligned $Na_{0.24}V_2O_5$ NWs on the substrate. The TEM image shows a single NW with the width estimated to be 80-100nm. The selected area electronic diffraction (SAED) pattern of a single wire recorded from [-1 3 1] zone axis reveals sharp and clean diffraction spots, indicative of single crystalline property (inset of Figure 3.2b). HRTEM image recorded from [-1 3 1] zone axis indicates lattice fringe of 3.48Å and 2.93Å, corresponding to (2 0 2) and (1 1 -2) crystal planes for $Na_{0.24}V_2O_5$, respectively. The growth direction along the a-axis is deduced from the angle of 155° between the a-axis and the normal vector of plane (1 1 -2), consistent with the previous studies.[51, 59]

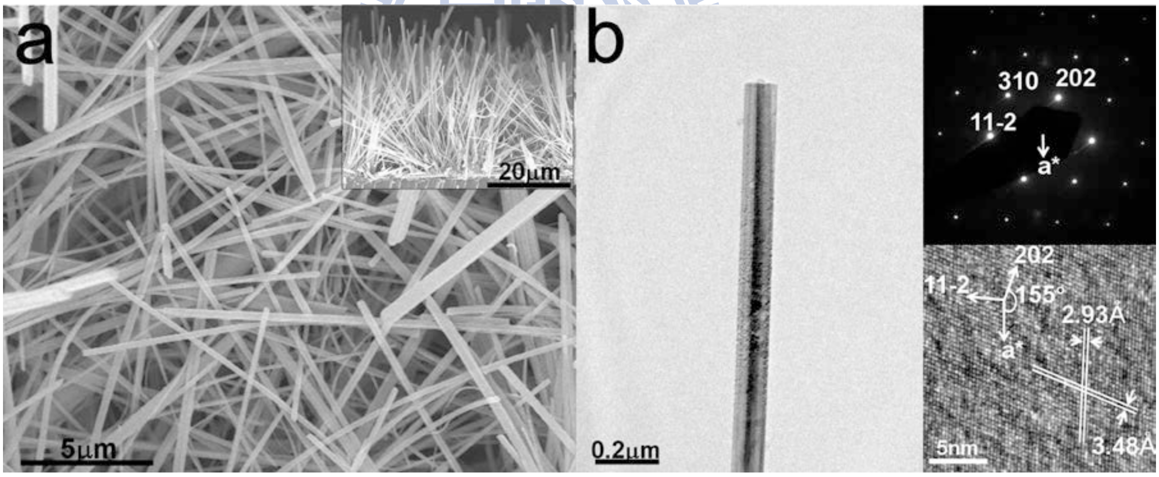

Figure 3.2 (a) Top view SEM image of $Na_{0.24}V_2O_5$ hin-film and side view in inset (b) TEM (left), SAED (right top), and HRTEM (right bottom) images of as-obtained $Na_{0.24}V_2O_5$ NWs.

3.3.3 X-Ray Photoelectron Spectroscopic Analyses

XPS measurements have been performed to study the information of oxidation states in the $Na_{0.24}V_2O_5$ NWs. As shown in Figure 3.3a, the spectrum demonstrates the presence of the elements of Na, V, and O. The spectrum for V-2p region (Figure 3.3b) shows binding energies (BE) of V $2p_{3/2}$ (516.15 eV) and V $2p_{1/2}$ (523.71 eV). The peak in V $2p_{3/2}$ spectrum exhibits a shoulder, indicative of mixed oxidation states of vanadium ion. After peak modeling, the V $2p_{3/2}$ spectrum contains two contributions at 516.9 eV and 515.4 eV corresponding to V^{5+} and V^{4+} ions; similar results can also be found in various ternary vanadium oxide bronze compounds.[46-47]

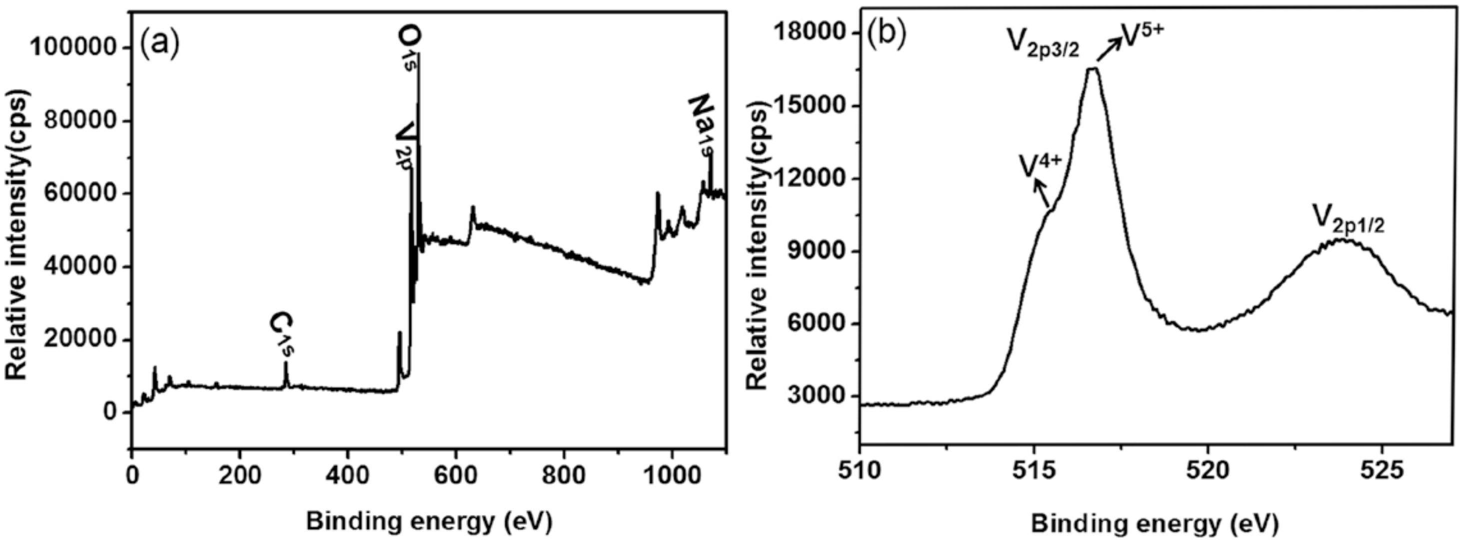

Figure 3.3 (a) Overall XPS spectrum and (b) high-magnification XPS spectrum for V-2p region of the NWs of $Na_{0.24}V_2O_5$

3.3.4 Optimization of Synthetic Condition

The coverage density and the average length of β-$Na_{0.24}V_2O_5$ NWs can be controlled by reaction temperature, the concentration of precursor solution and the concentration of sodium metasilicate during the thermal evaporation. To optimize the synthetic process, we tested several conditions to understand what factors affect the growth of $Na_{0.24}V_2O_5$ NWs, and the results are summarizes in Table 3.1 and Figure 3.4-3.6. Figure 3.4a-3.4c shows the effect of temperature to $Na_{0.24}V_2O_5$ NWs that were carried out at 300°C, 350°C, and 400°C, respectively. The average length of $Na_{0.24}V_2O_5$ wires increase with arising reaction temperature, and the film with the longest average length NWs was obtained at 400℃, similar to our previous study on the V_2O_5 and MoO_3 wires.[62-63] Notably, the coverage density of NWs increased as temperature arising, indicating that the temperature of deposition affect the amount of $Na_{0.24}V_2O_5$ nanocrystals created on the substrate. The spaces of NWs growth will be limited when the coverage density of NWs is high, resulting in the growth of nearly vertical NWs with no space to grow NWs along the horizontal orientation. For substrate with low coverage density of NWs, we observe randomly oriented NWs lying on the substrate. The results indicate that the length and amount of $Na_{0.24}V_2O_5$ NWs can be controlled by reaction temperatures. The substrates with preferred orientation of NWs can be observed in the samples synthesized at high temperature.

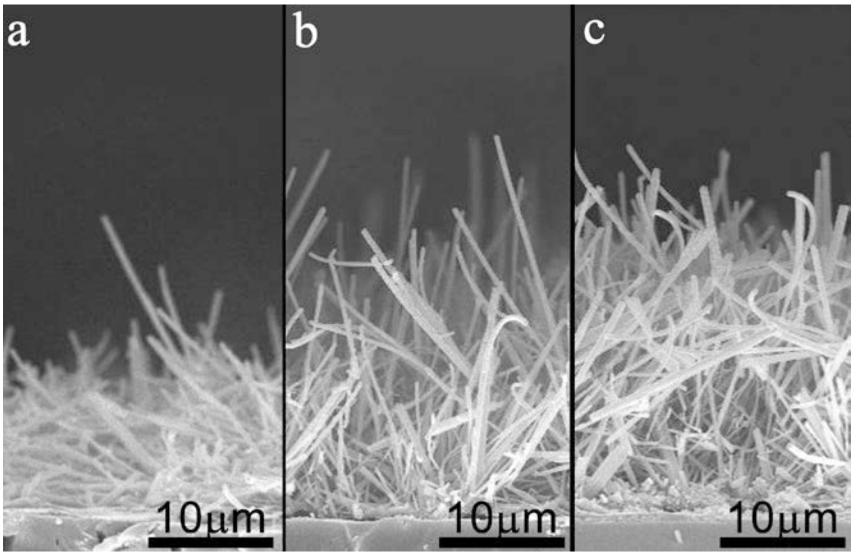

Figure 3.4 The side view images of as prepared $Na_{0.24}V_2O_5$ NWs thin-films synthesized at (a) 300°C, (b) 350°C and (c) 400°C, respectively.

The concentration of precursor solution and Na-solution are two additional factors that may affect the yield and morphology of the final product. For comparison, experiments with different concentration of the precursor solutions or sodium metasilicate solutions were prepared to synthesize $Na_{0.24}V_2O_5$ NWs while keeping other synthetic parameters unchanged. Figure 3.5 and 3.6 show the side view of NWs on substrates using different amount of precursor and sodium metasilicate. In general, all reactions yield wired shape of $Na_{0.24}V_2O_5$ NWs that are essentially independent of reaction temperature. For the effect of vanadium precursor, the average lengths of $Na_{0.24}V_2O_5$ NWs are 5.5, 23.1, and 30.5μm for concentration of 0.15, 0.3, and 0.45 M, respectively. For reactions with controlled amount of sodium metasilicate, the average lengths of $Na_{0.24}V_2O_5$ NWs are 12.2, 15.7, and 23.1μm for concentration of 0.0125, 0.025, and 0.05 M, respectively. The results indicate that the coverage density and length of NWs are affected by the concentration of the reactants (either precursor solution or sodium metasilicate solution). The reason for the evolution of NWs might be derived from the supply of reactants. The more the precursors are provided, the longer the growth of $Na_{0.24}V_2O_5$ NWs.

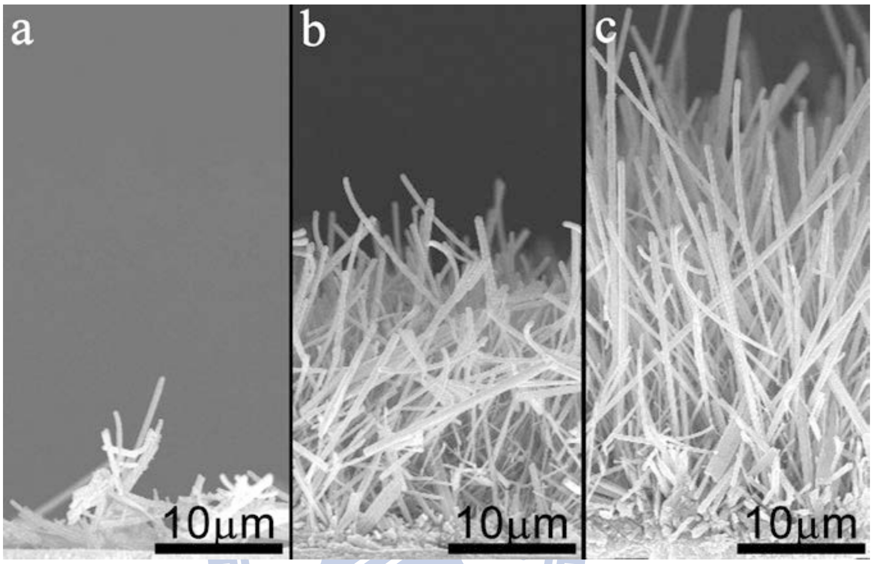

Figure 3.5 The side view images of as prepared $Na_{0.24}V_2O_5$ NWs thin-films synthesized by using precursor solution of concentration (a) 0.15M, (b) 0.30M and (c) 0.45M, respectively.

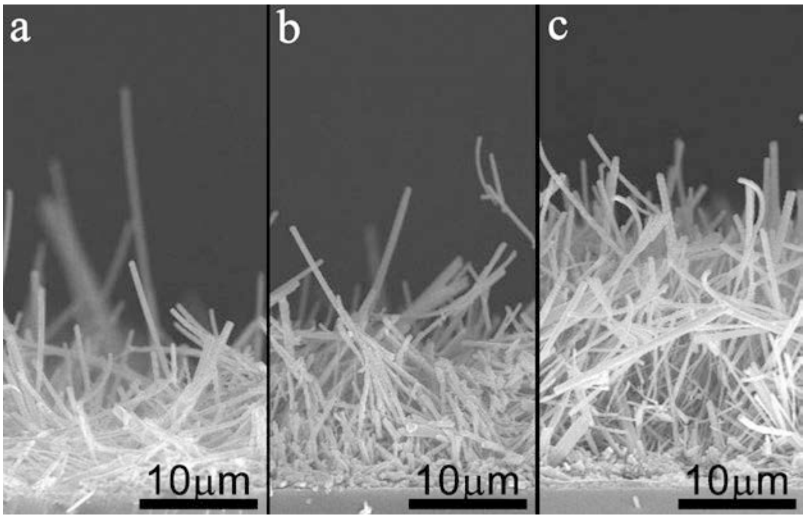

Figure 3.6 The side view images of as prepared $Na_{0.24}V_2O_5$ NWs thin-films synthesized by using Na-solution of concentration (a) 0.125M, (b) 0.025M and (c) 0.05M, respectively.

Table 3.1 Reaction conditions and morphology properties of $Na_{0.24}V_2O_5$ NWs identified with SEM

[Na- Solution]	[Precursor Solution]	Reaction temperature	Average length of nanowires
0.05M	0.3M	300°C	15±3 μm
0.05M	0.3M	350°C	20±4 μm
0.05M	0.3M	400°C	26±4 μm
0.05M	0.45M	400°C	37±5 μm
0.05M	0.15M	400°C	7±2 μm
0.025M	0.3M	400°C	15±4 μm
0.0125M	0.3M	400°C	13±3 μm

3.3.5 Formation Mechanism of As-Obtained $Na_{0.24}V_2O_5$ NWs

To understand the formation mechanism of as-prepared NWs, the evolution process was analyzed with XRD. The temperature of reaction was kept at 300 °C, which were terminated at definite reaction periods of 15, 30, and 45 minutes. The products were collected for XRD studies and the results are shown in Figure 3.7. For reaction terminated at 15 minutes, the XRD diffraction peaks can be indexed on the basis of the layered phase $V_2O_5{\cdot}xH_2O$, consistent with the previous studies.[21] For reaction ceased at 30 minutes, the product contains mixtures of $NaVO_3$ and $Na_{0.24}V_2O_5$. Finally, the product obtained from reaction period of 45 minutes could be identified as pure single phase of $Na_{0.24}V_2O_5$. On the basis of these results, we propose a reaction mechanism about the growth of $Na_{0.24}V_2O_5$ NWs, as shown in Figure 3.8.

During the initial stage of reaction, polyvanadate species (VO_x) were deposited on the substrate with the assistance of vapor transportation.[62] The polyvanadate species (VO_x) can be considered as mixtures of amorphous and crystalline phase of partially reduced vanadium oxide. At the initial stage, crystalline phase of $V_2O_5 \cdot xH_2O$ appeared. Thereafter, the sodium ions from sodium metasilicate were diffused and reacted to polyvanadate species (VO_x and $V_2O_5 \cdot xH_2O$) to form $NaVO_3$, which was further reacted to form the final product β-$Na_xV_2O_5$.[55] The β-$Na_xV_2O_5$ NWs will continue to grow as polyvanaate species and Na^+ ion gradually delivered to the seed crystals, resulting in the formation of β-$Na_xV_2O_5$ NWs. The crystal growth along [100] is affected by stacking of VO_x and the nature of β-$Na_xV_2O_5$.

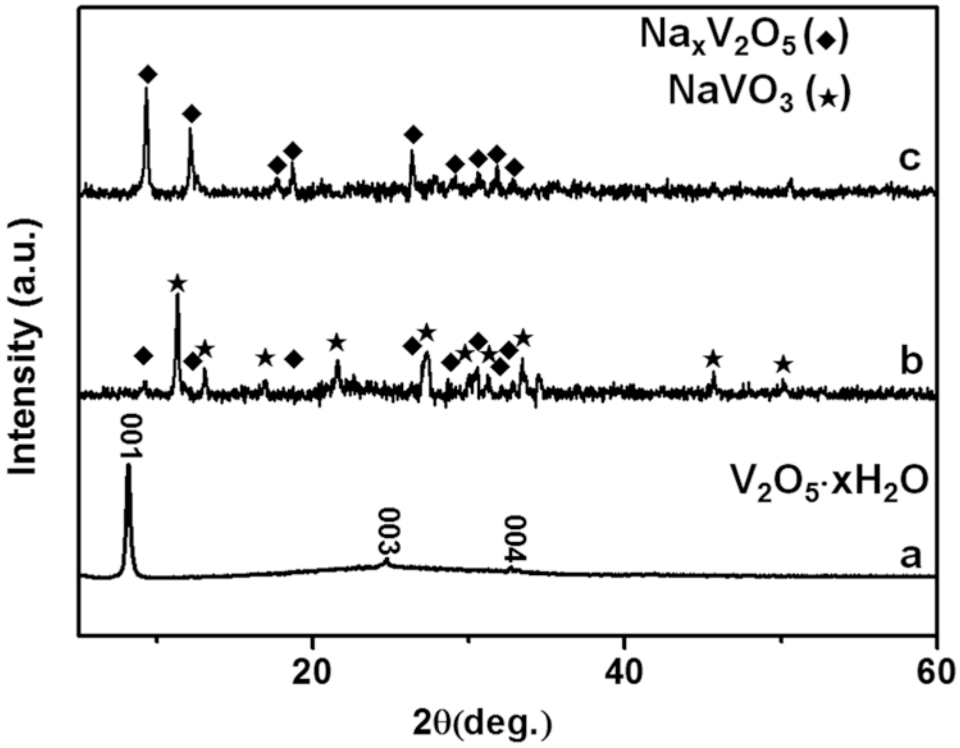

Figure 3.7 The XRD pattern of typical intermediate product synthesized at during period of (a) 15 minutes, (b) 30 minutes, (c) 45 minutes.

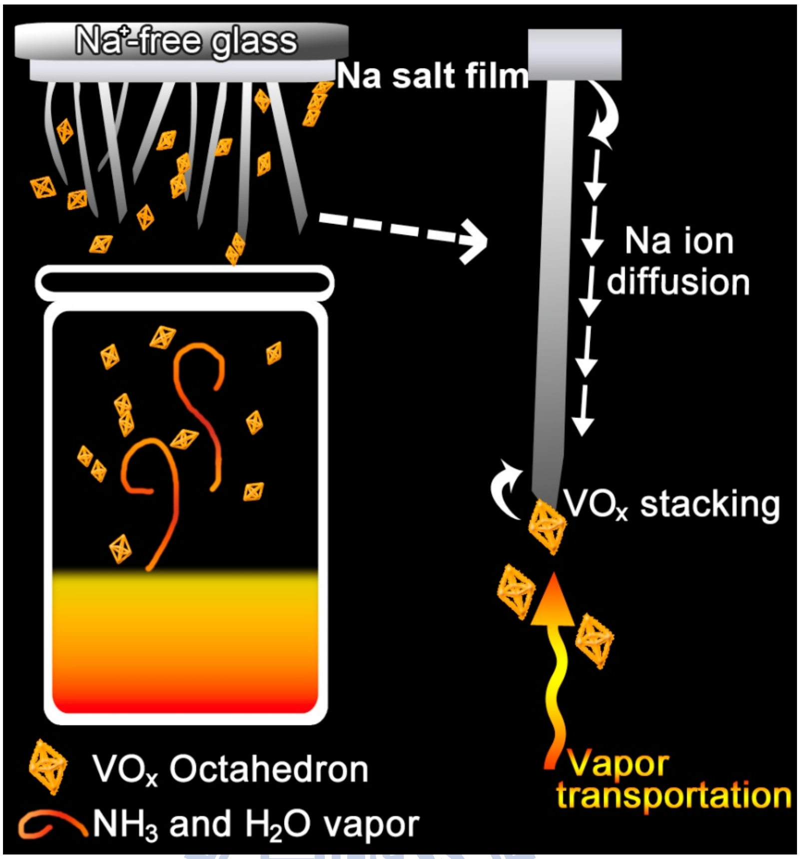

Figure 3.8 Schematic illustration of reaction mechanism to deposit β-$Na_xV_2O_5$ NWs on the surface of a substrate

3.3.6 Diffuse Reflectance Measurements

We measured the optical absorption to deduce the intrinsic optical properties of the $Na_{0.24}V_2O_5$ NWs aligned on glass substrate. Figure 3.9 shows the UV–visible absorption spectrum of the $Na_{0.24}V_2O_5$ thin-film that exhibits an onset of absorption near 500 nm, and the optical band gap (*Eg*) for the typical product is calculated from the absorption coefficient, α, using the relation $\alpha h\upsilon=A(h\upsilon-E_g)^{1/2}$ (*A*: constant; $h\upsilon$: energy of incident photon).[75-76] The inset of Figure 3.9 shows the plot of $(\alpha h\upsilon)^2$ versus photon energy $h\upsilon$, and the band gap of 2.18eV can be obtained by extrapolating the linear part of the graph to $\alpha h\upsilon$=0.

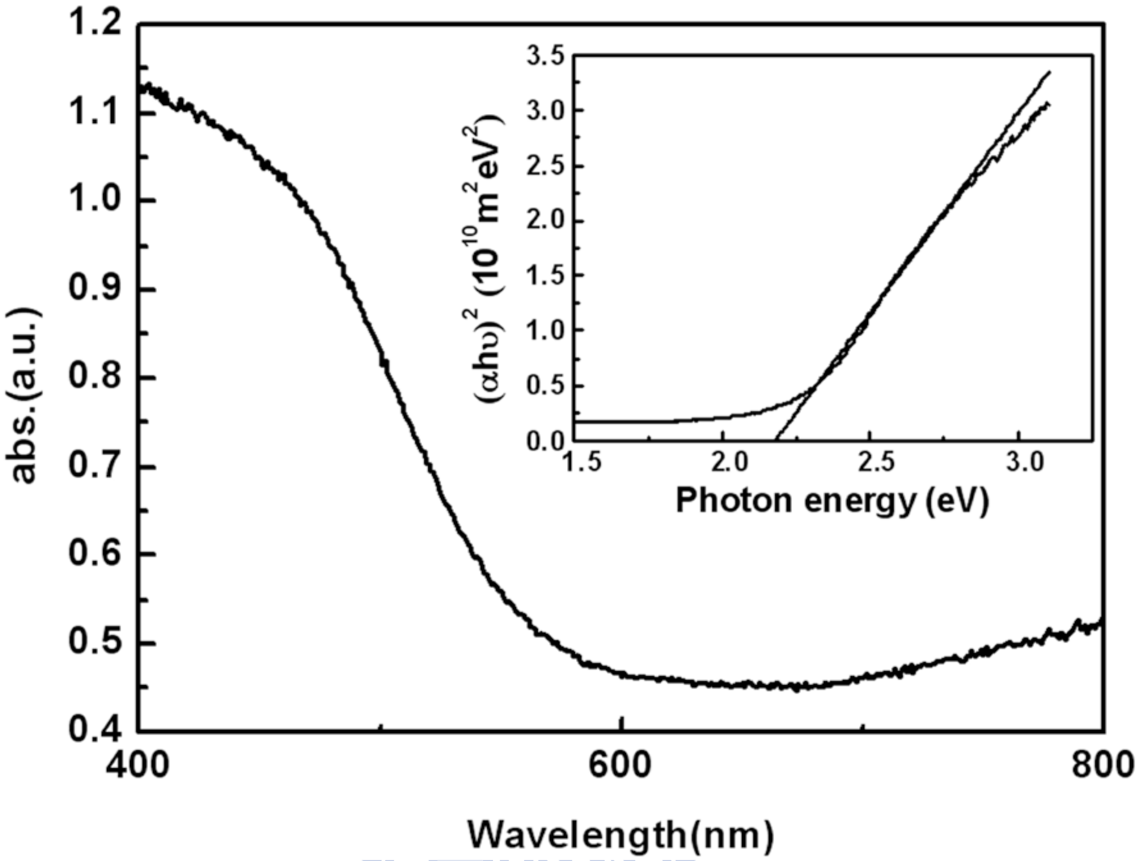

Figure 3.9. UV–visible absorption spectrum and the plot of $(\alpha h\upsilon)^2$ versus incident photon energy $h\upsilon$ (inset) for the $Na_{0.24}V_2O_5$ thin-film as prepared.

3.3.7 Electronic Field Emission Property.

The as-prepared films with nearly aligned $Na_{0.24}V_2O_5$ NWs may exhibit interesting field emission effect, which was measured with a parallel-plate configuration of electrodes near 295 K with a separation 100μm between the anode and an emitting surface of area 0.785mm^2. Figure 3.10 depicts the emission current density (J) versus an applied macroscopic field (E) within a ~0-1100V bias voltage range between the anode and samples. The turn-on field (E_{to}) about 7.8V/μm is defined as the macroscopic field required producing a current density of 10μA/cm^2. The FE current density can reach 4.66μA/cm^2 when the applied field increases to 11V/μm. The FE properties between thin-films of $Na_{0.24}V_2O_5$ and V_2O_5 NWs are summarized in Table 3.2. The value of the turn-on field in this study is higher than the results previously reported for vanadium oxide NWs.[62] The variations of the turn-on fields may be attributed to their crystal structure and chemical composition. A Fowler–Nordheim (F–N) plot of (ln I/E2) versus (1/E) appears in the inset of Figure 3.10; a linear relation indicates that the field emission from the film of $Na_{0.24}V_2O_5$ NWs conforms to the F–N theory and the emitted current is caused by quantum tunneling at the surface. [77]

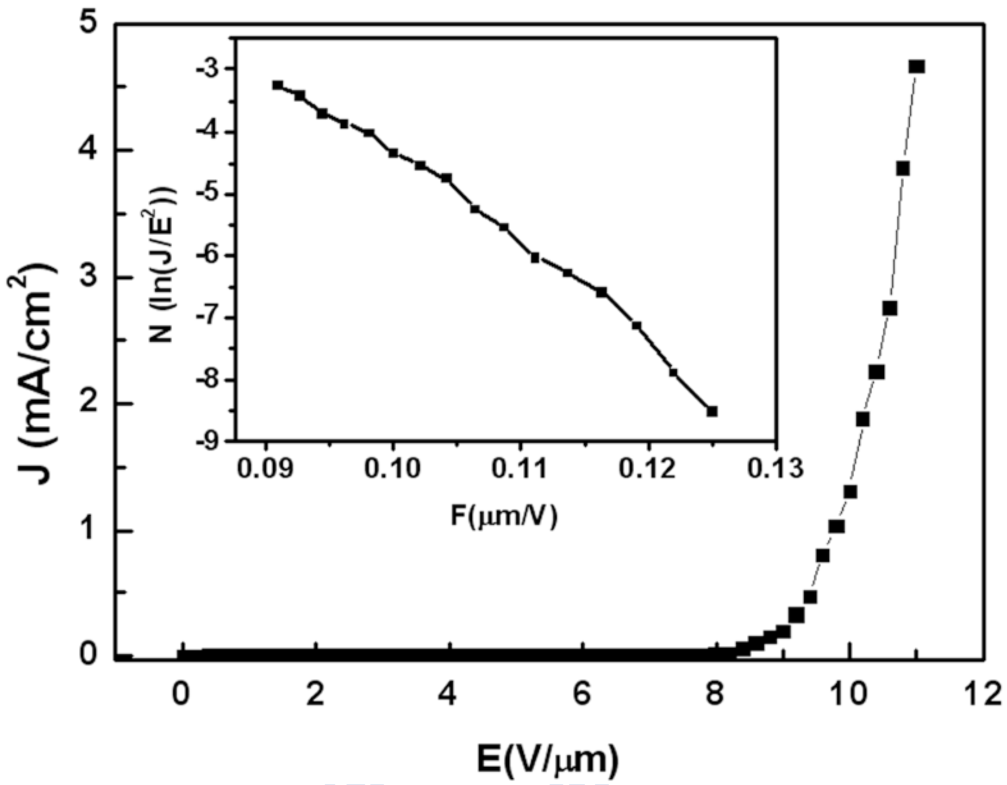

Figure 3.10 Field emission current density as a function of an applied electric field of as-prepared $Na_{0.24}V_2O_5$ NWs thin-film. Inset shows its corresponding Fowler-Nordheim plots.

Table 3.2 Comparison of FE properties between as-prepared product and V_2O_5 NWs

	E_{to}(V/μm)	I_{max}(mA/cm^2)
V_2O_5 NWs	8.3	1.8 at an applied field of 18V/μm
$Na_xV_2O_5$ NWs	7.8	4.66 at an applied field of 11V/μm

3.4 Summary

In this study, high quality and nearly aligned $Na_{0.24}V_2O_5$ NWs were fabricated via a simple, economical, mild, and template-free thermal evaporation method. The diameter and average length of NWs are 80-100nm and tens of micrometers, which grew along the [100] direction and tilted out of the glass substrate surface. A possible mechanism of crystal growth is proposed, and we also demonstrated that the distribution and length of NWs on thin film could be controlled by reaction temperature, concentration of precursor solution and sodium metasilicate. The as-obtained $Na_{0.24}V_2O_5$ NWs exhibit excellent field emission properties with a low turn-on field of 7.8 V/μm and a maximum current density of 4.66 mA/cm^2 at the applied field of 11.0 V/μm with linear F-N property, which might be used as field emission emitter. These results provide a new strategy to synthesize ternary inorganic NWs with great flexibilities in controlling the sizes, shapes, and coverage density of the NWs on different substrates. This unique synthetic route is expected to be applied to other aligned vanadium oxide bronze NWs, such as $M_xV_2O_5$ (M = K, Cu, Ag$_{)}$.

Chapter 4

Conclusions

In summary, binary phase (VO_2(R), VO_2(B), and V_2O_3) and ternary phase (β-$Na_xV_2O_5$) vanadium oxides nanowires have been successfully deposited and nearly vertically-aligned on the surface of substrate via two systematic procedure based on thermal evaporation. These as-prepared 1D nanomaterials possess diameter of 70-150nm and average length of tens micrometer, which grew and tilted on the surface of glass substrate surface with growth direction along specific direction of each product. The growth direction of the reduced products synthesized by post-reduction treatment, including VO_2(R), VO_2(B), and V_2O_3 nanowires, are affected by the growth of the original phase, V_2O_5 nanowires. Based on this concept, we propose the possible transformation mechanisms during the reduction treatment. On the other hand, the growth direction of β-$Na_xV_2O_5$ nanowires were examined along [1 0 0] direction, and the possible formation mechanism has also been discussed in detail.

The field emission properties of these binary and ternary vanadium oxides nanowires have been investigated. The as-prepared 1D nanomaterials exhibited excellent field emission performances which are highly dependent on their nature properties of crystal. Field emission properties of these as-prepared nanowires possessed low turn-on field, high emission current density and linear Fowler-Nordheim behaviors. Among these typical products, the lowest oxidation state of vanadium oxides, namely V_2O_3 nanowires, exhibit the best FE properties with E_{to} of 5.2 V/μm and J_{max} of 8.3 mA/cm^2 at the field of 8.3V/um. These remarkable results suggest that these 1D nanomaterials can be served as promising candidates for future field emission devices.

In this thesis, our study provided a novel synthetic procedure to deposit binary and ternary phase of vanadium oxide with nanostructure on the substrates, which are excellent for preparing metal oxide with 1D nanostructure owing to its utility advantages of simple, economic, time-saving and convenient for depositing thin-film on substrates. This unique synthetic route is anticipated to be applied to fabricate various binary and ternary phase metal-oxide nanocrystals well aligned on substrates with special crystal morphologies in choosing suitable precursors.

Reference

---

1. Ercolessi, F.; Andreoni, W.; Tosatti, E., *Phys.l Rev. Lett.* **1991,** *66*, 911-914.
2. Takagahara, T.; Takeda, K., *Phys. Rev. B* **1992,** *46*, 15578-15581.
3. Zhou, C.; Mai, L.; Liu, Y., et al., *J. Phys. Chem. C* **2007,** *111*, 8202-8205.
4. Chen, W.; Zhou, C.; Mai, L., et al., *J. Phys. Chem. C* **2008,** *112*, 2262-2265.
5. Melosh, N. A.; Boukai, A.; Diana, F., et al., *Science* **2003,** *300*, 112-115.
6. Santangelo, S.; Messina, G.; Faggio, G., et al., *Diam. Relat. Mater.* **2010,** *19*, 590-594.
7. Jiang, Y.; Zhang, W. J.; Jie, J. S., et al., *Adv. Mater.* **2006,** *18*, 1527-1532.
8. Li, X. L.; Cai, K. F.; Li, H., et al., *Superlattice. Microst.* **2010,** *47*, 710-713.
9. Sanmathi, C. S.; Takahashi, Y.; Sawaki, D., et al., *Mater. Res. Bull.* **2010,** *45*, 558-563.
10. Liu, A.; Ichihara, M.; Honma, I., et al., *Electrochem. Commun.* **2007,** *9*, 1766-1771.
11. Jiao, L.; Yuan, H.; Si, Y., et al., *Electrochem. Commun.* **2006,** *8*, 1041-1044.
12. Wang, Y.; Cao, G., *Electrochim. Acta* **2006,** *51*, 4865-4872.
13. Zhang, K.; Bao, S.; Liu, X., et al., *Mater. Res. Bull.* **2006,** *41*, 1985-1989.
14. Li, X.; Chen, X.; Chen, X., et al., *J. Cryst. Growth* **2007,** *309*, 43-47.
15. Wang, Y.; Cao, G., *J. Mater. Chem.* **2007,** *17*, 894.
16. Nayak, J.; Sahu, S.; Kasuya, J., et al., *Appl. Surf. Sci.* **2008,** *254*, 7215-7218.
17. Wang, Y. Q.; Zhang, Z. J.; Zhu, Y., et al., *Acs Nano* **2008,** *2*, 1492-1496.
18. Wang, K.; Chen, J. J.; Zeng, Z. M., et al., *Appl. Phys. Lett.* **2010,** *96*, 123105.
19. Li, L.; Liu, C.; Liu, Y., *Mater. Chem. Phys.* **2009,** *113*, 551-557.
20. Isabelle, R.; Marko, B.; Ulrich, S., et al., *Sensors Actuat. B- Chem.* **2005,** *106*, 730-735.
21. Liu, J. F.; Wang, X.; Peng, Q., et al., *Adv. Mater.* **2005,** *17*, 764.
22. Bakhteeva, Y. A.; Podval'naya, N. V.; Volkov, V. L., *Inorg. Mater.* **2010,** *46*, 1112-1114.
23. Grigorieva, A. V.; Badalyan, S. M.; Goodilin, E. A., et al., *Eur. J. Inorg. Chem.* **2010,** *2010*, 5247-5253.

24. Xiong, C. R.; Aliev, A. E.; Gnade, B., et al., *Acs Nano* **2008,** *2*, 293-301.

25. Ji, S.; Zhao, Y.; Zhang, F., et al., *J. Cryst. Growth* **2010,** *312*, 282-286.

26. Wang, Y.; Cao, G. Z., *Chem. Mater.* **2006,** *18*, 2787-2804.

27. Leger, C.; Bach, S.; Pereira-Ramos, J. P., *J. Solid State Electr.* **2007,** *11*, 71-76.

28. Ramana, C. V.; Smith, R. J.; Hussain, O. M., et al., *Surf. Interface Anal.* **2005,** *37*, 406-411.

29. Menezes, W. G.; Reis, D. M.; Benedetti, T. M., et al., *J. Colloid Interf. Sci.* **2009,** *337*, 586-593.

30. Leroux, C.; Nihoul, G.; Van Tendeloo, G., *Phys. Rev. B* **1998,** *57*, 5111-5121.

31. Morin, F., *Phys.l Rev. Lett.* **1959,** *3*, 34-36.

32. Richardson, M. A.; Coath, J. A., *Opt. Laser Technol.* **1998,** *30*, 137-140.

33. Nandakumar, N. K.; Seebauer, E. G., *Thin Solid Films* **2011,** *519*, 3663-3668.

34. Mathur, S.; Ruegamer, T.; Grobelsek, I., *Chem. Vapor Depos.* **2007,** *13*, 42-47.

35. Zhou, F.; Zhao, X. M.; Yuan, C. G., et al., *Cryst. Growth Des.* **2008,** *8*, 723-727.

36. Zhai, T.; Liu, H.; Li, H., et al., *Adv. Mater.* **2010,** *22*, 2547-2552.

37. Sediri, F.; Touati, F.; Gharbi, N., *Mater. Sci. Eng. B-Adv.* **2006,** *129*, 251-255.

38. Guiton, B. S.; Gu, Q.; Prieto, A. L., et al., *J. Am. Chem. Soc.* **2005,** *127*, 498-499.

39. Santulli, A. C.; Xu, W. Q.; Parise, J. B., et al., *Phys. Chem. Chem. Phys.* **2009,** *11*, 3718-3726.

40. Corr, S. A.; Grossman, M.; Furman, J. D., et al., *Chem. Mater.* **2008,** *20*, 6396-6404.

41. Zhou, F.; Zhao, X. M.; Yuan, C. G., et al., *Chem. Lett.* **2007,** *36*, 310-311.

42. Takahashi, K.; Limmer, S. J.; Wang, Y., et al., *Japanese Journal of Applied Physics* **2005,** *44*, 662-668.

43. Wu, X.; Tao, Y.; Dong, L., et al., *Mater. Res. Bull.* **2005,** *40*, 315-321.

44. Ji, S.; Zhang, F.; Jin, P., *Mater. Lett.* **2011,** *65*, 708-711.

45. Maeng, J.; Kim, T.; Jo, G., et al., *Mater. Res. Bull.* **2008,** *43*, 1649-1656.

46. Liu, Y.; Zhang, Y.; Zhang, M., et al., *J. Cryst. Growth* **2006,** *289*, 197-201.

47. Souza, E.; Lourenco, A.; Gorenstein, A., *Solid State Ionics* **2007,** *178*, 381-385.

48. An, J. N.; Xu, C. Y.; Zhen, L., et al., *Ceram. Int.* **2010,** *36*, 1825-1829.

49. Kong, L. F.; Shao, M. W.; Xie, Q., et al., *J. Cryst. Growth* **2004,** *260*, 435-439.

50. Liu, Y.; Zhang, Y. G.; Du, J., et al., *J. Cryst. Growth* **2006,** *291*, 320-324.

51. Liu, H.; Wang, Y.; Li, L., et al., *J. Mater. Chem.* **2009,** *19*, 7885.

52. Khoo, E.; Wang, J.; Ma, J., et al., *J. Mater. Chem.* **2010,** *20*, 8368.

53. Vasil'ev, A.; Marchenko, V.; Smirnov, A., et al., *Phys. Rev. B* **2001,** *64*.

54. Onoda, M.; Takahashi, T.; Nagasawa, H., *J. Phys. Soc. Jpn.* **1982,** *51*, 3868-3875.

55. Yamada, H.; Ueda, Y., *J. Phys. Soc. Jpn.* **1999,** *68*, 2735-2740.

56. Itoh, M.; Akimoto, N.; Yamada, H., et al., *J. Phys. Chem. Solids* **2001,** *62*, 351-354.

57. Yamauchi, T.; Ueda, Y.; Môri, N., *Phys.l Rev. Lett.* **2002,** *89*.

58. Zhou, G. T.; Wang, X. C.; Yu, J. C., *Cryst. Growth Des.* **2005,** *5*, 969-974.

59. Yu, J.; Yu, J. C., *Mater. Chem. Phys.* **2007,** *104*, 362-366.

60. Sahana, M. B.; Shivashankar, S. A., *J. Mater. Chem.* **2003,** *13*, 2254.

61. Sahana, M. B.; Dharmaprakash, M. S.; Shivashankar, S. A., *J. Mater. Chem.* **2002,** *12*, 333-338.

62. Wu, M. C.; Lee, C. S., *J. Solid State Chem.* **2009,** *182*, 2285-2289.

63. Wu, M. C.; Lee, C. S., *Mater. Res. Bull.* **2009,** *44*, 629-632.

64. Fowler, R. H.; Nordheim, L. W., *Proc. R. Soc. Lond. A* **1928,** *119*, 173-181.

65. Shen, X. P.; Yuan, A. H.; Hu, Y. M., et al., *Nanotechnology* **2005,** *16*, 2039-2043.

66. Li, Y. B.; Bando, Y.; Golberg, D., *Appl. Phys. Lett.* **2004,** *84*, 3603-3605.

67. Zhou, J.; Deng, S. Z.; Xu, N. S., et al., *Appl. Phys. Lett.* **2003,** *83*, 2653-2655.

68. Li, Y. B.; Bando, Y.; Golberg, D., et al., *Appl. Phys. Lett.* **2002,** *81*, 5048-5050.

69. Wang, J. B.; Li, K.; Zhong, X. L., et al., *Nanoscale Res. Lett.* **2009,** *4*, 1135.

70. Huang, Y.; Wang, Z. L.; Wang, Q., et al., *J. Phys. Chem. C* **2009,** *113*, 1980-1983.

71. Jeon, S.; Kim, H.; Yong, K., *Journal of Vacuum Science & Technology B: Microelectronics and Nanometer Structures* **2009,** *27*, 671.

72. Wang, S.; He, Y.; Fang, X., et al., *Adv. Mater.* **2009,** *21*, 2387-2392.

73. Xu, J. J.; Zhang, X. T.; Wang, D. J., et al., *Chem. Lett.* **2005,** *34*, 838-839.

74. B. Laugier, J. B. Celref, http://www.inpg.fr/LMGPS; Laboratoire des Materiaux et du Génie Physique de l'Ecole Supérieure de Physique de Grenoble.

75. Han, J.; Spanheimer, C.; Haindl, G., *Sol. Energ. Mat. Sol. C.* **2011,** *95*, 816-820.

76. Saipriya, S.; Sultan, M.; Singh, R., *Physica B* **2011,** *406*, 812-817.

77. Tang, Q.; Li, T.; Chen, X., et al., *Solid State Commun.* **2005,** *134*, 229-231.